Master degree course in Environmental and Land Engineering,
specialist pathway in Climate Change

Master Degree Thesis

Experimental study on the influence of vegetation on urban canyon ventilation

Supervisors:
Luca Ridolfi
Pietro Salizzoni
Sofia Fellini

Candidate:
Annika Vittoria Del Ponte

July 2022

Contents

Acknowledgements

Firstly, I would like to sincerely thank my supervisors, that gave me the opportunity to carry out an experience that allowed me to grow up both from an academic and a personal point of view. I thank Professor Luca Ridolfi who proposed this thesis, and who was always precise, careful and available for providing ideas and explanations, and for helping me to manage the whole work. I thank Professor Pietro Salizzoni for welcoming me to the École Centrale de Lyon for the whole year, and for always being ready to provide new and encouraging ideas for the development of the project. I am very grateful to Sofia Fellini who shared with me part of her research work and part of her knowledge, and who closely helped, encouraged and motivated me, with great patience and enthusiasm. I thank Massimo Marro who followed me with enthusiasm and patience during the whole experimental campaign inside the wind tunnel.

Furthermore, I would like to infinitely thank Jean, Livia, Raffaello, Fabio, Marilina, Cosimo, Andrea, Jheyson, Stefano with whom I had the pleasure of sharing moments of work and leisure, in Lyon. They were able to create a friendly and stimulating atmosphere. In particular, a special thank to Cosimo for always being ready to spur me and support me in any situation.

I would like to sincerely thank Alberta, Andrea, Anna, Edoardo, Laura, Lorenzo, Marta, Laura, Elisa, Nicolò, Riccardo, Roberta, Livia, who accompanied me during my path at Politecnico di Torino. They started to believe in me before that I started to believe in myself. They have shared with me days of crazy study and moments of crazy fun, making these five years at Polito unforgettable.

The last but not the least, I express all my gratitude to my family for having always believed in me, and in particular to my parents, who never said "no" to me, and who always did the impossible to make me happy.

Abstract

The greening of cities is one of the most encouraged mitigation strategies to face the urban heat island phenomenon, as vegetation increases the evapotranspiration and the shading. Moreover, trees concur to improve the air quality of cities, as they enhance the pollutant deposition rate thanks to their large surface area. However, few studies on the impact of tree planting on the natural ventilation and dispersion mechanisms inside urban street canyons are available. In the present thesis, we report the results of an experimental campaign performed in the wind tunnel facility of École Centrale de Lyon, aimed at understanding how the presence and the density of trees affect the air exchange between the urban street canyon and the external atmosphere, and if it hinders the pollutant removal mechanisms.

For this purpose, concentration, velocity, and combined concentration and velocity measurements have been performed inside a street canyon, without street intersections, oriented perpendicular to the wind direction, inserted in an urban network reproduced inside the test section of the wind tunnel. The vehicular pollution has been simulated by a linear source of ethane, which behaves as a passive scalar. The aerodynamic behavior of trees has been reproduced by inserting plastic miniatures along the two long sides of the canyon, using four different trees density configurations: absence of trees inside the canyon, two rows of one tree positioned on the central axis of the canyon, two low density tree rows, and two high density tree rows.

Results show that the concentration field is essentially two-dimensional in the empty cavity configuration, reveling that the dispersion phenomenon is governed by recirculating cells that transport the pollutant from the downwind wall to the upwind wall, while it becomes three-dimensional in all the configurations with trees, meaning that there are further recirculating cells along the longitudinal direction of the canyon. The presence of trees modifies the spatial distribution of the pollutant concentration, but has a low impact on the bulk vertical exchange velocity, which has almost the same values in the four configurations. From the velocity measurements, we find that the presence of trees decreases the turbulent kinetic energy and it homogenizes the mean vertical velocity. Combined measurements of concentration and velocity allow turbulent mass fluxes to be evaluated, both inside

the canyon and at the rooftop. Comparing the mass fluxes with the concentration field, it is found that inside the canyon the turbulent component of the total mass flux is responsible for the mixing of the pollutant in the case without trees, while it is almost negligible in the case with trees. At the rooftop, the mean mass flux has the highest contribution in both cases. The statistical analysis of concentration time series measured in different spatial points inside the canyon reveals that the dispersion phenomenon can be entirely modeled with a Gamma distribution, even if the Lognormal and the Weibull 2p distributions perform a good fitting as well, and that the extreme concentration events are governed by an exponential law.

The experimental campaign highlights that vegetation modifies the concentration and the velocity fields inside the street canyon, but the constant value of vertical exchange velocity suggests that the overall ventilation efficiency is not decreased. Moreover, the fine three-dimensional grid on which concentration measurements are organized provides a huge database of concentration data to validate numerical models that simulate the dispersion of a passive scalar into empty and vegetated street canyons.

Sommario

L'inserimento della vegetazione nelle città è una delle strategie di mitigazione più ambite per far fronte al fenomeno dell'isola di calore urbana, dal momento che la vegetazione aumenta l'evapotraspirazione e protegge il suolo dal sole. Inoltre, gli alberi contribuiscono a migliorare la qualità dell'aria delle città, poichè promuovono la deposizione di inquinanti, grazie alla loro grande superfice. Tuttavia, sono disponibili pochi studi riguardo all'impatto degli alberi sulla ventilazione naturale e sui meccanismi di dispersione che avvengono all'interno di un canyon urbano. In questa tesi, vengono riportati i risultati di una campagna sperimentale svolta nella galleria del vento dell'École Centrale de Lyon, con l'obbiettivo di capire come la presenza e la densità degli alberi influenzi il ricambio d'aria tra la strada e l'atmosfera esterna, e se essa impedisca i meccanismi di rimozione degli inquinanti.

Con questo obiettivo, sono state svolte misure di concentrazione, velocità e misure accoppiate di concentrazione e velocità, all'interno di un canyon urbano, senza incroci, orientato perpendicolarmente rispetto alla direzione del vento, inserito nel reticolo urbano riprodotto all'interno della sezione di misurazione della galleria del vento. L'inquinamento automobilistico è stato simulato con una sorgente lineare di etano, che si comporta come uno scalare passivo. Il comportamento aereodinamico degli alberi è stato riprodotto inserendo modellini di alberi in plastica lungo i due lati lunghi del canyon, secondo quattro differenti densità di alberi: canyon senza alberi, due file con un albero in corrispondenza dell'asse centrale del canyon, due file con bassa densità di alberi, e due file con alta densità di alberi.

I risultati mostrano che il campo di concentrazione è essenzialmente bidimensionale nella configurazione con il canyon vuoto, e questo rivela che il fenomeno di dispersione è governato da celle ricircolanti che trasportano l'inquinante dalla parete di valle alla parete di monte, mentre esso diventa tridimensionale in tutte le configurazioni con gli alberi, dimostrando che ci sono ulteriori celle ricircolanti lungo la direzione longitudinale del canyon. La presenza di alberi modifica la distribuzione spaziale della concentrazione di inquinante, ma ha un basso impatto sulla velocità di scambio di massa verticale, la quale presenta circa gli stessi valori nelle quattro configurazioni. Dalle misure di velocità vediamo che la presenza di alberi diminuisce l'energia cinetica turbolenta e omogenizza la velocità media verticale. Misure accop-

piate di concentrazione e velocità permettono di stimare i flussi di massa turbolenti, sia all'interno del canyon che al tetto. Confrontando i flussi di massa con il campo di concentrazione vediamo che all'interno del canyon la componente turbulenta del fusso di massa totale è responsabile del mescolamento dell'inquinante nel caso senza alberi, mentre essa è quasi trascurabile nel caso con gli alberi. Al tetto, il flusso di massa convettivo ha il maggiore contributo in entrambi i casi.

L'analisi statistica delle serie temporali di concentrazione, misurate in punti differenti nello spazio all'interno del canyon, rivela che il fenomeno di dispersione può essere interamente modellizzato da una distribuzione Gamma, anche se le distribuzioni Lognormale e di Weibull 2p mostrano un buon accordo, e che gli eventi estremi sono governati da una legge esponenziale.

La campagna sperimentale evidenzia che la vegetazione modifica i campi di concentrazione e velocità all'interno del canyon, ma il valore costante di velocità di scambio verticale suggerisce che l'efficienza di ventilazione globale non è diminuita. Inoltre, la griglia tridimensionale fine su cui sono state organizzate le misure di concentrazione fornisce un grosso volume di dati per validare i modelli numerici che simulano la dispersione di uno scalare passivo in un canyon vuoto e con vegetazione.

Introduction

Cities are the center of economic development and technological innovation. They provide opportunities for jobs, culture and entrantainement. Nowadays, 55% of the World's population lives in urban areas, and this percentage is expected to increase to 68% by 2050, as reported by the United Nations. However, the increasing urbanization causes radical changing in the characteristics of the surface, resulting in the modification of heat, mass and momentum exchange between the surface and the atmosphere. The high rates of human activities and vehicular displacement produce high levels of Green House Gasses emissions in the atmosphere. According to the report of EEA (European Environment Agengy), in 2020, 96% of the urban population, in Europe, was exposed to concentrations of $PM_{2.5}$ above the WHO annual limit, 71% to over-limit concentrations of PM_{10}, 95 % to over-limit concentrations of O_3, and 89% to over-limit concentrations of NO_2.

The most relevant environmental problem linked to cities is the urban heat island. It is defined as the increase of the atmospheric temperature in the urban environment with respect to the surrounding rural areas. This effect is triggered by several factors, like the low albedo of the infrastructure materials, the urban geometry, the reduction of the temperature mitigation due to vegetation evapotranspiration, and domestic heat emissions. The urban heat island causes negative effects on citizens' thermal comfort and health and on biodiversity. The impermeabilization of the surface increases the surface water runoff, making the cities vulnerable to weather extreme events, that are more and more frequent due to climate change. Cities are the drivers of economic exercises and represent the fulcrum of human activities and social relations, therefore, their sustainable development and the improvement of the quality of life are included in one of the sustainable development goals of the United Nations (SDG11).

One of the most encouraged mitigation strategies, to reduce the impact of global warming on cities' temperature, their vulnerability to extreme events and urban air pollution, is the greening of the cities. Vegetation leads to several environmental benefits in urban areas (Ferrini et al., 2020). Trees are fundamental for temperature regulation inside cities, as they provide shading, they enhance evapotranspiration, and they reduce the heat radiated from the ground, being characterized by an

albedo lower than the one of the building materials. All these effects contribute to the mitigation of the urban heat island and to the reduction of energy consumption for cooling purposes. Tree crowns act as sinks of pollutants as they promote polluted air filtration, and particle dry deposition, thanks to the large surface area of the leaves. Small size particles and gaseous pollutants could be removed through stomata absorption. Moreover, photosynthesis guarantees CO_2 removal from the air. Tree planting increases the amount of permeable surface in cities and it increases the infiltration capacity of urban surface. This guarantees the availability of soil moisture for evapotranspiration and the regulation of stormwater runoff, and consequently a reduction of flooding risks. Finally, green areas guarantee human and ecosystem well-being: they provide the presence of natural areas for amusement, increase biodiversity, and attenuate noise pollution, as the complex structure of tree crowns causes degradation of sound waves.

The positive effects of vegetation on the sustainable management of the urban environment are deeply investigated, while few studies on the adverse effect of vegetation on street ventilation and pollutant dispersion are available. What is known is that the vegetation inserted inside street canyons reduces the flow velocity, so vertical exchange between the external atmosphere and the canyon is weakened, and that traffic pollution accumulates at pedestrian level (Abhijith et al., 2017). Of course, to assess the problem it is necessary to consider several factors like wind direction with respect to the street, tree characteristic, tree spacing, and street geometry.

In this work, we analyze the influence of tree avenues on ventilation and pollutant dispersion inside a street canyon oriented perpendicular to the external wind flow direction. These aspects are investigated through an experimental campaign performed in the atmospheric wind tunnel of École Centrale de Lyon. Different vegetation densities will be analyzed: the empty canyon case, medium vegetation density and high vegetation density. Concentration, velocity and mass fluxes measurements will be performed, in order to analyze the dispersion of a passive scalar inside the canyon, to characterize the flow field, and to analyze the principle transfer mechanisms that govern the vertical pollutant transfer between the canyon and the external flow. The instrumentation involved are the Flame Ionization Detector (FID), for concentration measurements, the Laser Dopler Anemometer (LDA), for velocity measurements, and the system LDA-FID, for turbulent mass fluxes measurements.

The thesis is divided into three main chapters. In chapter 1, we present the state of the art of the problem: the description of the flow structures that generate when a current interacts with an urban network, previous experimental and numerical studies on the influence of vegetation on concentration and flow fields in urban canyons and previous experimental campaigns in the wind tunnel of École Centrale de Lyon. In chapter 2, we describe the wind tunnel and the atmospheric boundary

layer developed inside the test section, the characteristics of the vegetation and the measurement instruments. In chapter 3 the results of the entire experimental campaign are shown. The latter chapter is divided into two parts: the first one is dedicated to the analysis of time averaged quantities, namely concentration field, velocity field and mass fluxes, and the second one is dedicated to time series analysis, namely we perform statistical analysis of concentration time series and spectral analysis of turbulent mass and momentum fluxes.

Chapter 1

State of the art and theoretical concepts

1.1 Flow and dispersion in the Urban Boundary Layer

Pollutant dispersion in the urban environment is governed by flow structures which are generated by the interaction between the atmospheric boundary layer and the urban canopy. The Atmospheric Boundary Layer is the part of the atmosphere in direct contact with the Earth's surface, thus its physical behavior is affected by mass, momentum and heat fluxes between the two environmental sectors. When an air current interacts with urban areas, it perceives the increase in the surface roughness, due to the presence of buildings, and the increase in the surface temperature, due to human activities, lower albedo of the building materials, and decrease in evapotranspiration. Neglecting the thermal effects and assuming neutral stratification, the mean flow field along the vertical direction is divided into two different regions: the inertial region and the roughness sub-layer (figure 1.1a).

In the inertial region, the flow perceives the presence of buildings as a unique element of homogeneous roughness. The mean velocity profile is assumed homogeneous on the horizontal plane, and it is described with the wall logarithmic law:

$$\frac{\overline{U}}{u_*} = \frac{1}{\kappa} ln(\frac{z-d}{z_0}) \tag{1.1}$$

where $\overline{U}$ is the mean horizontal velocity, u_* is the friction velocity, κ is the von Karman constant, z is the vertical coordinate, d is the displacement height and z_0 is the roughness length, or rather the height of the surface irregularities. The introduction of the d parameter guarantee the upward displacement of the horizontal plane where the flow velocity is zero (figure 1.1b), as the logarithmic law is not valid

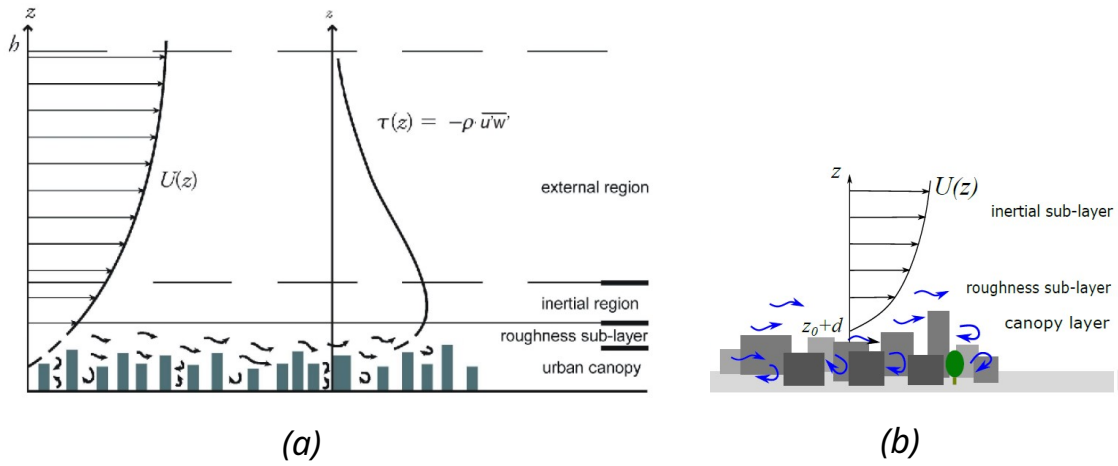

Figure 1.1: *(a) Vertical structure of the atmospheric boundary layer above the urban canopy (Cancelli et al., 2006). (b) Logarithmic wind profile at the city scale (Fellini, 2021).*

within the urban canopy, due to the presence of recirculating structures between obstacles.

In the roughness sub-layer, the urban canopy is no more represented as a unique obstacle with homogeneous drag. The flow field is no more homogeneous along the horizontal plane, but it is affected by the position and orientation of buildings with respect to the wind direction. Considering a wind direction perpendicular to the urban canopy, three different kinds of flow regimes can be distinguished, according to Oke (2002) (figure 1.2), depending on the density of buildings, which is expressed by the streets aspect ratio H/W (where H is the building height and W is the along-wind spacing). If the obstacles are sufficiently spaced apart ($H/W < 0.35$) the current recovers its undisturbed conditions before investing a second obstacle. The flow pattern between the two obstacles appears to be the same as if they were isolated, thus the regime is called *isolated roughness flow regime*. At closer spacing ($0.35 < H/W < 0.65$), the transition to a *wake interference flow regime occurs*, due to the fact that the current cannot recover its initial conditions before investing the second obstacle, thus the wakes generated by the single obstacles interact. When the spacing is further decreased ($H/W > 0.65$), there is no more interaction between the atmospheric flow and the canyon one. A single recirculating structure is generated between the obstacles, and the *skimming flow regime* is established. With different wind directions, the flow regime is even more complex: if the wind is parallel to the street, the current enters the canyon generating a channeling phenomenon, if the wind is oriented with an angle the channeling is coupled with recirculation and a helical flow pattern is generated.

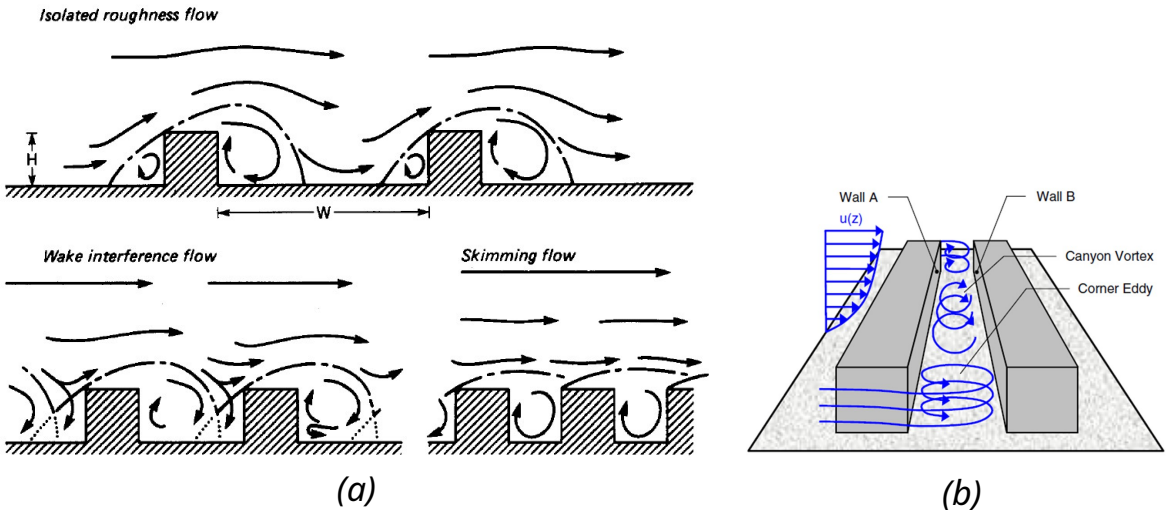

Figure 1.2: *(a) Flow regimes associated with different urban geometries (Oke, 2002). (b) Flow structures inside a urban street canyon (Gromke and Ruck, 2009).*

To study pollutant dispersion mechanisms inside the urban canopy, it is necessary to focus on the interaction between the pollutant emitted at the ground level, due to vehicular traffic, and the flow structures which are generated between buildings. The urban complexity is schematized by the urban street canyon, represented as a street of width W bounded by two buildings of height H (figure 1.2b). Its geometry is described by the H/W ratio. When it is oriented perpendicular to the atmospheric flow, two kinds of recirculating flow structures can be identified: the canyon vortex in the center of the canyon, and the corner eddies at the edges. The canyon vortex is the dominant structure of the flow field inside the street canyon. It is formed due to the interaction between the external atmospheric flow and the street canyon walls: the airflow enters the canyon at the downwind wall, at the ground level it is deflected toward the upwind wall, where part of it goes outside the canyon and part is entrained toward the downwind wall. This air circulation provokes a greater accumulation of pollutants toward the upwind wall. The corner eddies provide additional air exchange at the canyon sides, but their contribution is significant only up to a length of 3.5 W (Gromke and Ruck, 2009).

1.2 Influence of vegetation

Vegetation inserted within urban canyons may act as obstacles to air ventilation and pollutant dispersion mechanisms, as from the aerodynamic point of view trees are porous objects that may produce changes in drag and wakes to the airflow that crosses their crowns. The effect of tree avenues on the flow and concentration

fields inside urban street canyons has been investigated mainly with wind tunnel experiments and CFD simulations. Gromke and Ruck (2007) performed a first experimental campaign inside an isolated street canyon with a row of model trees with spherical crowns placed along the center axis. They found that, if a wind flow perpendicular to the canyon is considered, the presence of trees causes an increase of pollutant concentration at the pedestrian level at the upwind wall, as trees inhibit the upward flow, and a decrease at the downwind wall, due to the fact that tree crowns hinder the re-entrainment of the flow from the upwind wall to the downwind one. Moreover, the lateral air exchange promoted by corner eddies is significantly reduced, resulting in an overall increase of the pollutant concentration inside the canyon. The changes of concentration induced by trees were found to be more pronounced with higher vegetation density, or rather with greater tree crown diameter and smaller tree spacing. The influence of crown porosity has been studied as well, in a second experimental campaign (Gromke and Ruck, 2009), where the tree avenue has been modeled with a lattice cage filled with filament synthetic wadding material of different densities. The results revealed that the influence of the crown porosity on the concentration variations is remarkable only if the pore volume is greater than 97 %. Moreover, velocity measurements show that the presence of a central tree avenue does not destroy the canyon vortex structure, but it reduces the upward and downward flow velocities, resulting in a weakening of the air circulation inside the canyon. By setting different directions of the approaching wind flow (Gromke and Ruck, 2012), it has been found that the presence of tree avenues does not influence the pollutant concentration in the case of wind flow parallel to the street canyon axis, and that with a wind flow inclined 45° with respect to the canyon axis the walls averaged concentration is lower with higher vegetation density, as a more packed vegetation enhances the street axis channeling of the flow.

The experimental data, acquired in the street canyon with two rows of trees modeled with the lattice cage, has been used to validate RANS simulations (Gromke et al., 2008; Buccolieri et al., 2009). Numerical simulations reproduce well the flow and concentration fields detected during the experimental campaign, as well as the relative difference in the spatial distribution of the concentration between empty and vegetated street canyons. However, high concentration values at the upwind wall are slightly underestimated, while the lower ones at the downwind wall are well estimated.

On the trail of the studies of Gromke and Ruck (2007, 2009, 2012), the aerodynamic behavior of vegetation inside urban street canyons has been analyzed using the wind tunnel facilities, built in the École Centrale de Lyon. Tree avenues have been modeled arranging plastic small-scale trees in two parallel rows inside the canyon. Different vegetation densities have been reproduced placing the trees with different spacing. De Giovanni (2019) studied the influence of vegetation density

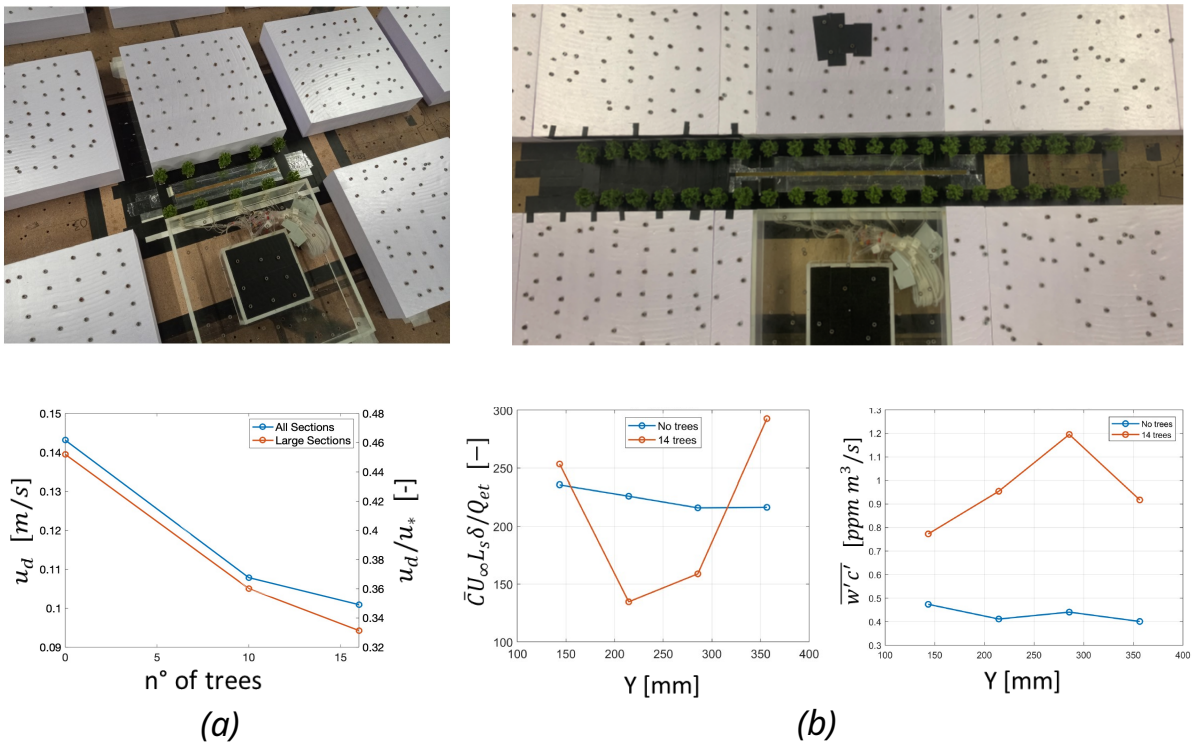

Figure 1.3: *(a) Urban street canyon with street intersections (above). Variation of the vertical exchange velocity with respect to the number of trees, from De Giovanni (2019) (below). (b) Urban street canyon with open edges, without street intersections (above). Variation of the mean concentration and of the turbulent mass fluxes at the rooftop in the longitudinal direction of the canyon, from Balestrieri (2021) (below).*

and wind direction on the dispersion of passive scalar within a street canyon of $H/W = 0.5$, with street intersections (figure 1.3a). With the wind blowing perpendicular to the canyon, the results found in the studies cited above have been confirmed: lower pollutant concentration at the downwind wall and higher one towards the upwind wall, decrease in concentration towards the edges due to the action of the corner eddies, overall increase of pollutant concentration, mostly at the upwind wall and canyon edges, with the increase of tree density. The rotation of the model street canyon 60° with respect to the wind direction leads to an accumulation of the pollutant at the downwind edge of the canyon. The presence of trees seems to reduce the longitudinal ventilation, but the influence of the tree density is no more detectable. The overall concentration inside the rotated canyon is half the one measured inside the canyon oriented perpendicular to the wind direction.

Moreover, the estimation of the efficiency of the ventilation inside the street canyon has been performed calculating the vertical exchange velocity (defined as u_d). Assuming steady-state conditions inside the canyon and that the vertical exchange velocity and the lateral one are equal, the mass transfer velocity between the canyon and the external flow, with a perpendicular wind direction, has been extracted from the following mass balance:

$$Q_{et} = u_d CLW + 2(u_d CWH) \tag{1.2}$$

where Q_{et} is the ethane flowrate emitted inside the canyon from a linear source on the ground, C is the spatial mean concentration, L is the length of the control volume, W is the width of the canyon and H its height. It has been found that u_d decreases with the increase of the number of trees, meaning that vegetation reduces the ventilation efficiency of the canyon (see figure 1.3a). However, the contribution of the lateral inflows is not negligible for the dilution of pollutants inside the canyon, thus neglecting the contribution of the lateral mean flow to the street canyon ventilation constitutes an inaccurate estimation of the u_d, especially in the empty canyon.

To avoid lateral interactions between the external flow and the canyon flow, a street canyon, oriented perpendicular to the wind direction, without street intersections has been analyzed in a second experimental campaign (Balestrieri, 2021). Here, the vertical exchange velocity at the rooftop of the canyon has been calculated in a direct way, performing coupled velocity-concentration measurements. The u_d has been calculated as:

$$u_d = \frac{1}{LWC} \int_A (\bar{w}\bar{c} + \overline{w'c'}) dA \tag{1.3}$$

where $\bar{w}\bar{c}$ is the mean mass flux, $\overline{w'c'}$ is the turbulent mass flux, A is the area of the rooftop of the canyon. By numerically integrating the total mass flux at the rooftop, they found that the presence of trees enounces the vertical flow rate. This

result, opposite to the expectations, has been attributed to the fact that without trees there is a non-negligible lateral outflow, which decreases the overall vertical flow. This hypothesis has been verified, as the expected decrease of u_d in presence of trees has been obtained by imposing that the existing vertical flowrate is equal to the entering one, neglecting any lateral mass exchange. Looking at the variation of the mean passive scalar concentration along the longitudinal direction in the canyon, it has been observed that the concentration field is bi-dimensional in the no-trees configuration, while it is three-dimensional when trees are inserted. This result has been reconducted to the inhomogeneity of the total vertical mass flux in the case of the vegetated canyon: it is maximum in the center of the canyon, where the mean concentration presents a minimum, and it decreases moving towards the canyon edges, where an accumulation of pollutant has been found (figure 1.3b).

The uncertainty of the estimation of the vertical mass fluxes and the interesting result obtained comparing the concentration fields of the empty canyon with the one of the vegetated canyon, have promoted a further experimental campaign inside a street canyon, again oriented perpendicular to the wind direction, confined both laterally and longitudinally. This configuration is the subject of the present thesis.

Chapter 2

Experimental facilities and working methods

2.1 Experimental setup

The experimental measurements have been carried out in the recirculating wind tunnel of the *Laboratoire de Mecanique des Fluides et d'Acoustique* (LMFA), at École Centrale de Lyon. It is an infrastructure where atmospheric dispersion in boundary layers can be investigated. For the present experimental campaign, an urban atmospheric boundary layer has been reconstructed.

In the upper part, there is an axial fan, which generates wind velocities between 0.5 m/s and 6 m/s, a diverging system and a converging system, and in the lower part there is the test section (figure 2.1a). The test section is 12 m long, 2 m high and 3.5 m wide. The floor is covered by blocks of wood and blocks of polystyrene spaced apart, to simulate the urban buildings and street intersections (figure 2.1b). The blocks are spaced 10 cm along the longitudinal direction and 20 cm along the lateral direction. The longitudinal streets are narrower to avoid flow channeling, which can hinder the development of a homogeneous boundary layer, above the building roofs. For the same purpose, transversal blocks have been inserted at some street intersections at the entrance of the test section. The roughness of the roofs is reproduced with steel bolts 5 mm high, randomly placed on the top of the blocks (figure 2.2a).

The reference street canyon (figure 2.2b) is a closed cavity 1 m long, 10 cm high and 20 cm wide, guaranteeing an aspect ratio (H/W) equal to 0.5. It is placed perpendicular to the wind direction. In the middle of the cavity, a linear source, 65 cm long and 1 cm wide, continuously emits a mixture of 3.8 l/min of air and 0.2 l/min of ethane (C_2H_6). Ethane has been chosen as a tracer since it has a density similar to air, so the ethane behaves as a passive scalar. The ethane source can be assimilated to any linear source of pollutants inside the urban environment, as a

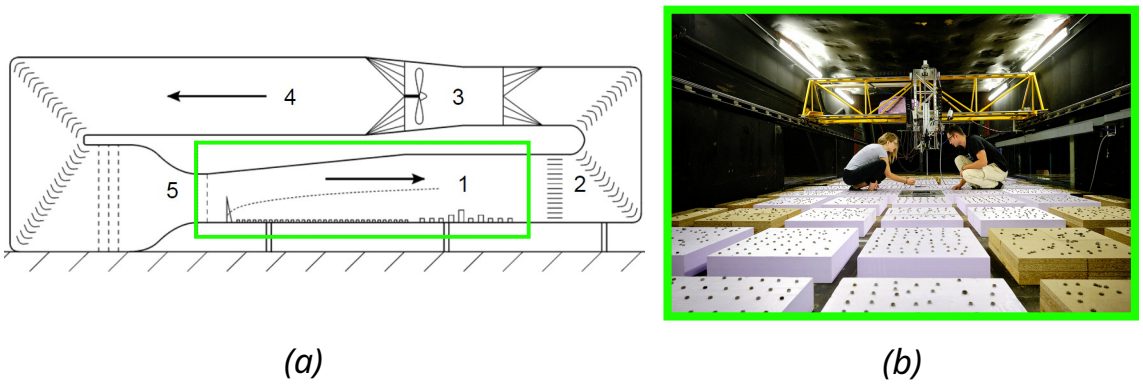

Figure 2.1: *(a) Scheme of the wind tunnel: 1 test section; 2 heat exchanger system; 3 fan; 4 diverging system; 5 converging system and generating turbulence grid. (b) Street network simulated inside the test section.*

traffic jam for example. It is worthy to note that the source length does not cover the entire length of the cavity. The reference system considered has the origin (X=0 mm, Y=0 mm, Z=0 mm) in the middle of the street canyon, at the upwind wall: the X coordinate increases according to the streamwise direction, the Y coordinate is oriented perpendicular to the streamwise direction, along the length of the canyon, and the Z coordinate increases from the floor level (Z=0 mm) towards the top of the model buildings (Z=100 mm).

A wind flow is generated by the fan installed in the upper part of the wind tunnel, above the test section. The wind flow is perturbed by a turbulent grid, which generates homogeneous turbulence, and a row of 7 Irwin spires, both placed at the entrance of the test section. The combination of the grid and the spires, and the rough blocks on the floor (Irwin, 1981) guarantees a fully developed boundary layer of depth (δ) 1.1 m. In the present experiment, the velocity of the fan, which determines the constant wind velocity in the upper part of the boundary layer (U_∞), is maintained at 5 m/s. It is controlled by a Pitot tube, which measures the velocity by linking it to the difference between the total pressure and the static pressure, and the fluid density, through the Bernulli's principle. The pressure values are measured by a differential manometer placed outside the test section.

The characteristics of the boundary layer developed inside the test section of the wind tunnel have been defined in the previous experimental campaign performed by Balestrieri (2021). He performed velocity measurements inside the test section at different longitudinal distances from the entrance. By averaging the wind profiles measured in four different points at each distance considered, he verified that the boundary layer is fully developed in the whole test section. Moreover, by exploiting the velocity correlation profiles ($\overline{u'w'}$) measured above the reference street canyon, which define Reynolds shear stress, the parameters that outline the logarithmic wind

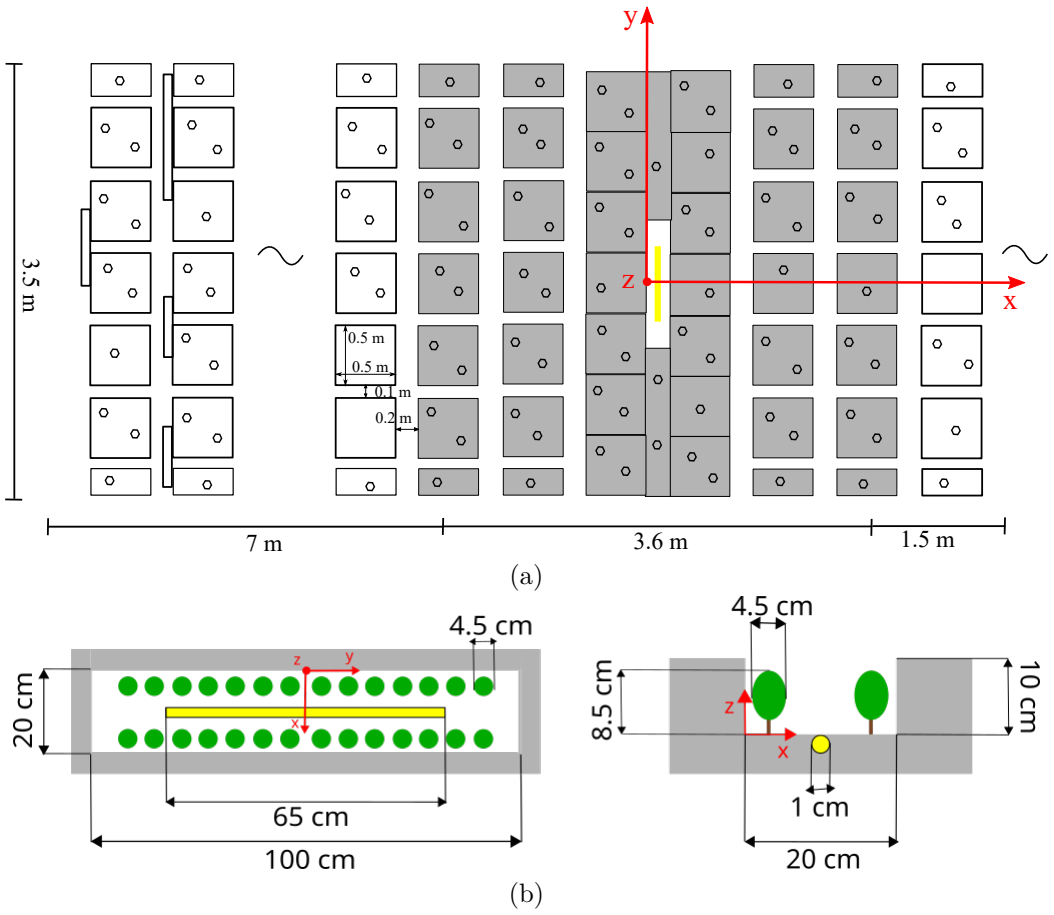

Figure 2.2: *(a) Plan of the urban network constructed inside the test section. (b) Plan (on the left) and frontal view (on the right) of the reference street canyon with trees.*

profile have been defined. In the interval where Reynolds stresses are constant, a friction velocity (u_*) of 0.23 m/s has been calculated, and, by linearly interpolating the velocity profile in that interval with a logarithmic law, a roughness length (z_0) of 0.21 mm and a zero-plane displacement (d) of 96 mm have been retrieved. However, we have to consider that U_∞ was 5.3 m/s, slightly different from the one of the present study. Knowing that the shape of the boundary layer is the same in both experimental campaigns, the ratio u_*/U_∞ (equal to 0.043) remains constant. As in the present campaign U_∞ is 5 m/s, we obtain that u_* is equal to 0.22 m/s.

The urban vegetation is simulated through plastic miniatures of trees (namely, the ones used for railway modeling), which have a trunk of 2 cm and a porous canopy, made of plastic filaments, 6.5 cm high and 4.5 cm wide. Their aerodynamic behavior has been characterized in terms of aerodynamic porosity and drag coefficient. The aerodynamic porosity has been evaluated in two different ways (reported by De Giovanni (2019) and Fellini (2021)): by measuring the wind velocity upwind and downwind the tree and doing the ratio between them, and by applying the empirical relation which links the aerodynamic porosity to the optical one, defined by processing images depicting the silhouette of the tree. In both cases, an aerodynamic porosity of around 0.3 has been obtained. The drag coefficient has been measured inside a small closed circuit wind tunnel, equipped with a load cell that measures the force exerted by the wind on the model trees. The drag coefficient has been measured considering different wind velocities and Reynolds numbers, and it has been observed that it converges at a constant value for wind velocities greater than 5 m/s. Following this procedure, a drag coefficient of 0.75 has been retrieved (Fellini, 2021). The model trees are inserted in the reference cavity, arranged according to four different configurations: no trees inside the canyon (Zero configuration. Figure 2.5a), two parallel rows of one tree in the middle of the canyon (One-tree configuration. Figure 2.5b), two parallel rows of seven equally spaced trees (Half configuration. Figure 2.5c) and two parallel rows of fourteen equally spaced trees (Full configuration. Figure 2.5d). Concentration measurements in Zero and Full configurations have been retrieved from Mechinaud (2021).

2.2 Measured variables and instruments

2.2.1 Concentration field

Concentration measurements inside the reference street canyon have been performed using a Flame Ionization Detector (FID) (figure 2.3). It measures the concentration of an organic compound, by detecting the ions produced during its combustion. The mixture of air and ethane released by the linear source is sucked inside the FID through a sampling capillary tube 30 cm long, and it is burned by an internal flame,

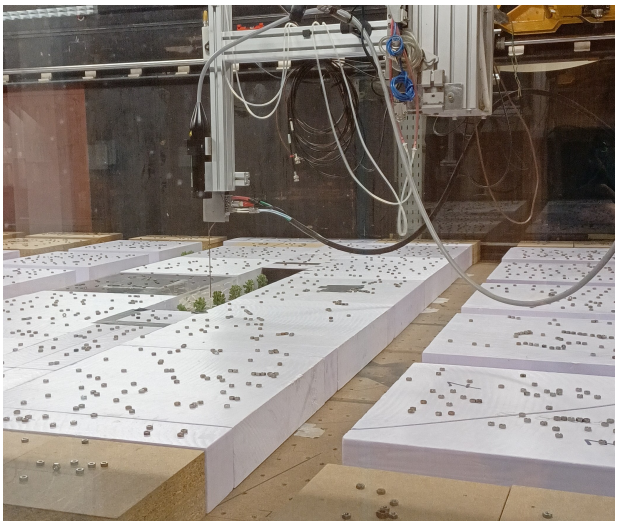

Figure 2.3: *Concentration measurements inside the reference street canyon using Flame Ionization Detector.*

fed by hydrogen and oxygen. The combustion induces the decomposition of the ethane into positive ions and electrons, which are detected by two electrodes, anode and cathode, promoting the generation of a current proportional to the ionization rate. The output of the instrument is an electric potential measured in Volt, which has a linear relation with the concentration of ethane.

To determine the slope of the linear function, which allows the voltage to be converted into concentration evaluated in ppm, it is necessary to calibrate the instrument twice: a first time before the beginning of the measurement session and a second time at its end, to verify that the slope coefficient has maintained the same value (a variation of $\pm 3\%$ is accepted). The second calibration can be anticipated if the temperature of the flame of the FID varies more than 2 °C from its initial value. This is necessary because the instrument performance is sensitive to variations in the flame temperature. Operatively, the calibration is performed by measuring with the FID the concentration of four ethane-air mixtures with concentrations equal to 0, 500, 1000 and 5000 ppm. The measured concentrations, expressed in Volt, are plotted with respect to the known concentration values, expressed in ppm, and they are interpolated with a linear function. The slope coefficient obtained is inserted in the FC2D-FID software, which acquires the measurements from the FID, and it is maintained during the whole measurement session. The FID has a precision between 0-10 volt, and it can detect concentration values between 5 and 5000 ppm.

The FID measures with a constant frequency of 1000 sample/s. The duration of the acquisition windows has been stated by studying the convergence of the mean and the variance of the instantaneous concentration signal, at different measurement

points along the cavity without trees. Both the statistical parameters have been calculated for progressively larger groups of instantaneous measurements ($\overline{C}_{\mathrm{n}}$, ${\sigma_{\mathrm{c,n}}}^2$) and respectively normalized over their final total value ($\overline{C}$, ${\sigma_{\mathrm{c}}}^2$). We have perfect convergence of the measurement when the ratio tends to 1 for a long interval of additional samples. Looking at figure 2.4, we notice that the convergence of both the statistics presents a maximum deviation of around 10% from the unity, if an acquisition time of 120 s is considered. Such error decreases considering other different points. From this result, it has been stated that setting an acquisition time of 120 s allows us to reach an acceptable convergence of the statistical moments, and to perform a huge number of measurements spending an acceptable amount of time. The acquisition time will be prolonged at 300 s, in order to collect a higher number of data, to perform statistical studies on concentration time series, which will be presented in Chapter 3.

As the wind tunnel is a recirculating system, an accumulation of pollutant could occur, leading to an increase in the background concentration with time, that may cause an overestimation of the concentration measured in the canyon. For this reason, before starting each measurement, the source is automatically stopped for 15 s, to let the canyon empty, and then the instrument measures for 15 s the background concentration. The same operation is repeated at the end of each measurement. A linear interpolation between the initial and the final background noise is performed by the software, and the result is subtracted from the instantaneous concentration measurements.

Concentration measurements have been organized in transversal sections, acquired along the Y direction. They are composed of 45 measurement points when they cover the entire width of the cavity, and of 15 measurement points when they lay between two trees. In figure 2.5 we can see the measurement grids used in the four different configurations, to characterize the mean concentration field inside the cavity. They are repeated along the vertical direction at heights Z=20, 40, 60, 80, 100 mm. Moreover, a single concentration profile in the middle of the cavity (X=100 mm, Z=40 mm) has been acquired with the acquisition time window of 300 s.

2.2.2 Velocity field

To characterize the velocity field inside the reference canyon a Laser Doppler Anemometer (LDA) has been used (figure 2.6). It is an optical instrument that measures the velocity of particles transported inside a fluid, by illuminating them with a laser beam of known frequency, and by acquiring the reflected light. As the particles are in motion, the scattered light has a different frequency compared to the transmitted one, according to the Doppler effect; the difference in frequency, called Doppler shift, is proportional to the velocity of the particle. The LDA is equipped with an

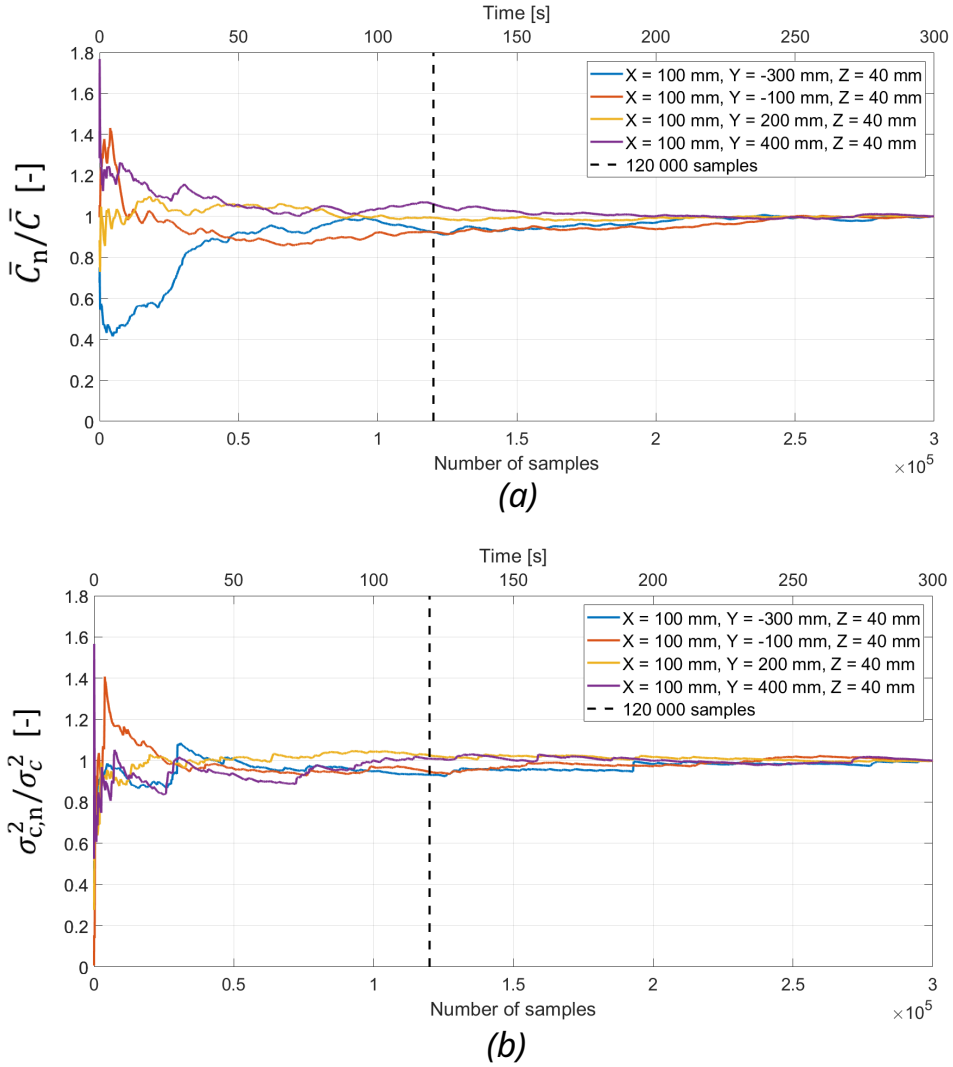

Figure 2.4: *(a) Convergence of the mean concentration signal; (b) convergence of the variance of the concentration signal. The dotted line stands for the acquisition time window of the FID chosen for concentration measurements.*

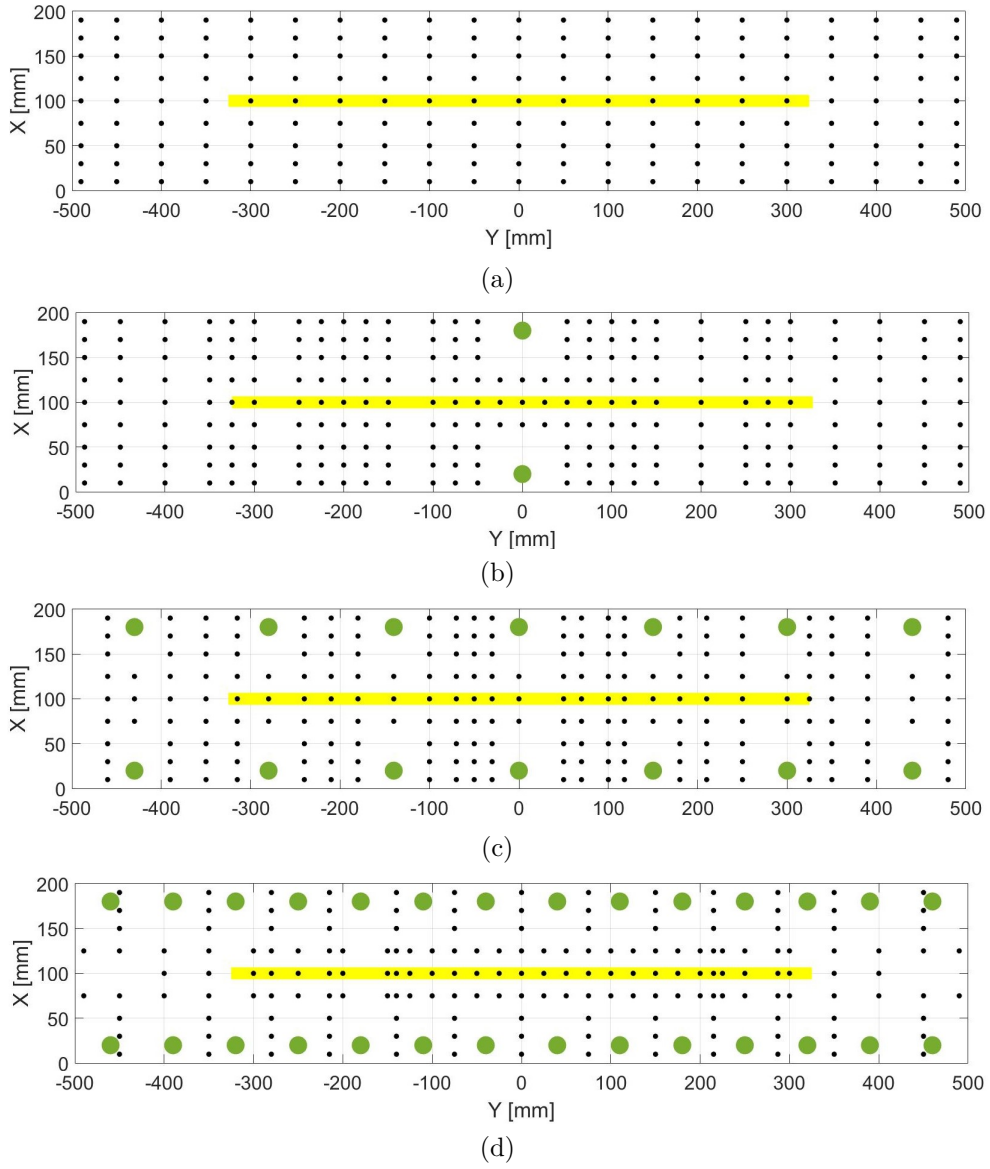

Figure 2.5: *(a) Zero configuration measurement grid; (b) One-tree configuration measurement grid; (c) Half configuration measurement grid; (d) Full configuration measurement grid. The green dots represent the trees, the yellow line represents the linear source.*

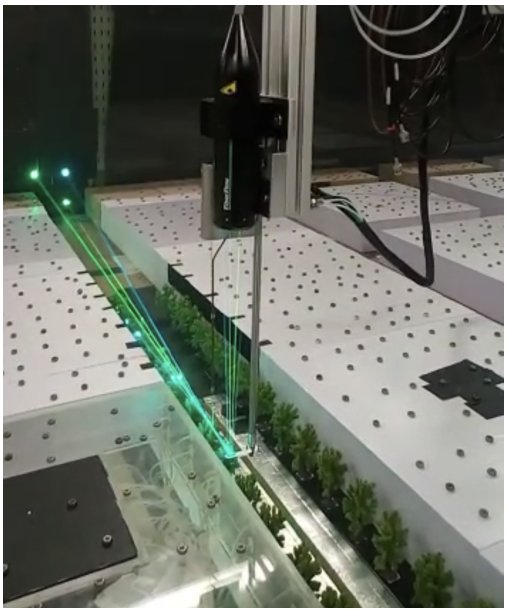

Figure 2.6: *LDA performing measurements in the open cavity with trees.*

optical system that emits two laser rays, one with the characteristic wavelength of the blue and the other with the characteristic wavelength of the green, which are in turn split into two beams. The four laser beams, emitted by a probe inside the LDA, intersect in a point, which defines the measuring volume. The light scattered from the particle is collected by the photodetector, which transforms it into an electrical signal, that will be pre-processed and converted into a velocity measurement through the Burst Spectrum Analyser (BSA). The two laser beams with different colors provide the module and the direction of two velocity components: the one in the streamwise direction (u) and the one perpendicular to the wind direction (v). To know the vertical component of the velocity (w), it is necessary to combine the LDA with a mirror, that deflects the scattered laser beam. Inside the test section, a fog flow (namely the one used as show smoke) is spread, in order to make the air opaque, to promote reflection, and to provide tracing particles. The smoke machine is placed at the end of the test section, downstream with respect to the canyon, in a way that the smoke goes through the recirculating system of the wind tunnel and is homogenized.

As the measurement occurs when particles intercept the intersection point of the four beams, the acquisition frequency of the instrument is not constant, but it depends on the particle arrival time. Moreover, small and faster particles are detected more frequently than big and slower ones, thus an overestimation of the mean and the variance arises. To obtain a correct estimation of the statistical moments, it is necessary to weigh them with the particle transit time, which is a

proper factor since it is inversely proportional to the velocity (Tropea et al., 2007). With the purpose of studying the convergence of statistical moments, the weighted mean of the u velocity component has been evaluated through the equation:

$$\overline{U}_n = \frac{\sum_{i=1}^{n} u_i \cdot tt_i}{\sum_{i=1}^{n} tt_i} \tag{2.1}$$

where u is the instantaneous velocity, tt is the particle transit time, n is the number of samples considered in each interval, and the weighted variance has been calculated as:

$$\sigma^2_{u,n} = \frac{\sum_{i=1}^{n} (u_i - \overline{U})^2 \cdot tt_i}{\sum_{i=1}^{n} tt_i} \tag{2.2}$$

where $\overline{U}$ is the total mean velocity. In figure 2.7 it is possible to notice that the acquisition of 250 000 particles is suitable to obtain good convergence of both the mean and the variance of the u velocity component. The same result has been obtained for the longitudinal and vertical velocity components, applying the same procedure.

Velocity measurements have been acquired over a central vertical section, according to five longitudinal profiles at different heights, Z=20, 40, 60, 80, 98 mm. It was not possible to measure the velocity on a grid as refined as the one used for concentration measurements, because the vegetated canyon cannot host the mirror (used to measure the w component), so inside it is possible to measure velocity between the two rows of trees only.

2.2.3 Vertical mass fluxes

Coupled measurements of concentration and velocity have been carried out to obtain the estimation of turbulent mass fluxes ($\overline{w'c'}$). At each measurement point, the LDA is combined with the FID, to collect simultaneously the vertical component of the velocity (w) and concentration data (c). A scheme of the configuration is available in figure 2.8a. During the acquisition, the ethane source is turned on, and the smoke machine as well. The FID and the LDA are forced to begin and finish the measure at the same time, therefore an acquisition time of 200 s has been set for both of them. It is known that over that time the FID can acquire 200 000 instantaneous measurements, so it is necessary to manually control the sensitivity of the LDA to guarantee approximately the same acquisition frequency. The convergence of the mean, weighted for the transit time, of the coupled signal has been calculated as:

$$\overline{w'c'}_n = \frac{\sum_{i=1}^{n} w'_i \cdot c'_i \cdot tt_i}{\sum_{i=1}^{n} tt_i}. \tag{2.3}$$

Looking at figure 2.9 we can say that an acquisition time of 200 s produces a sufficient amount of instantaneous concetration and velocity values to guarantee the convergence of the statistics of the correlated signal.

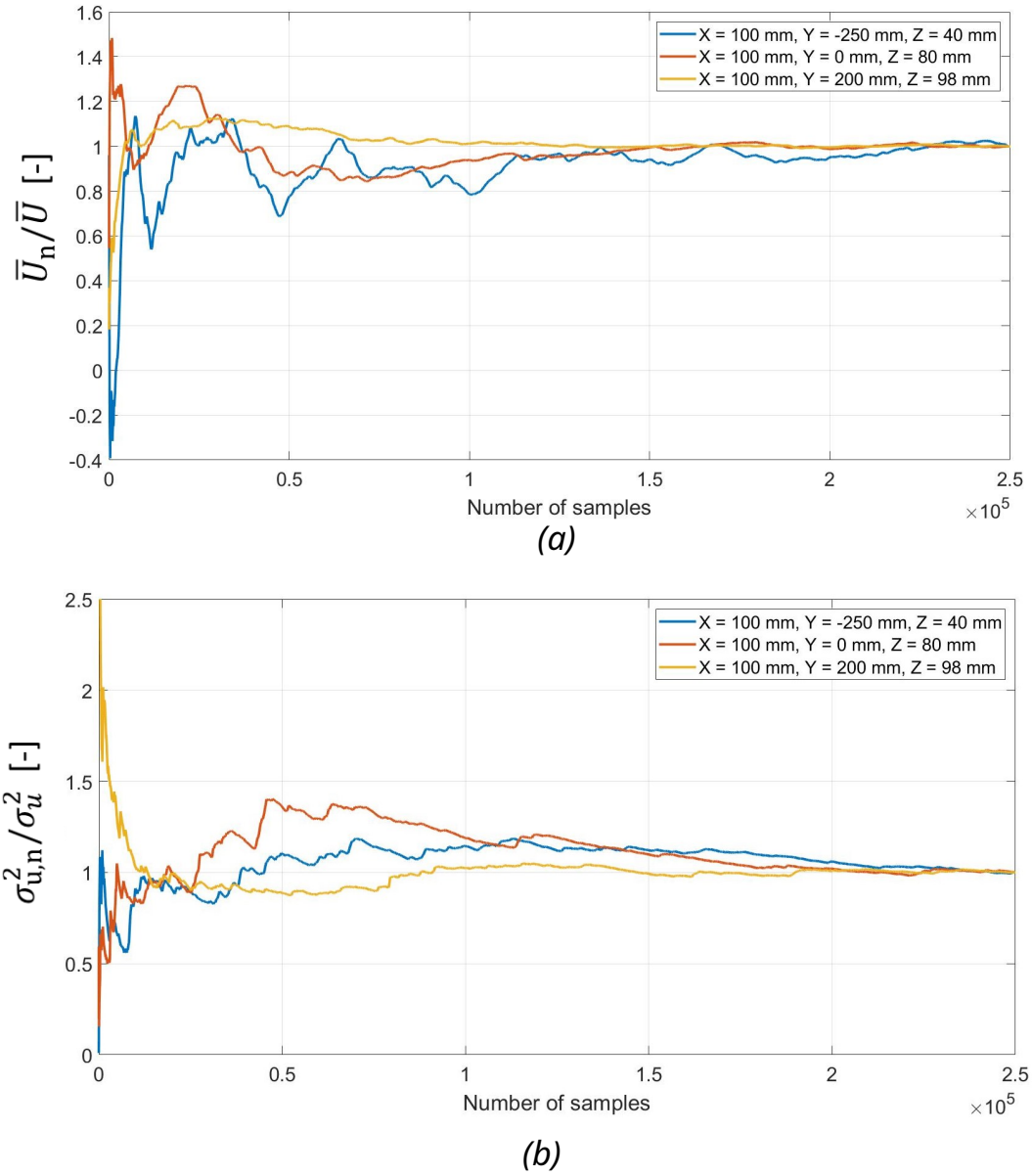

Figure 2.7: *(a) Convergence of the mean of the u velocity component; (b) convergence of the variance of the u velocity component.*

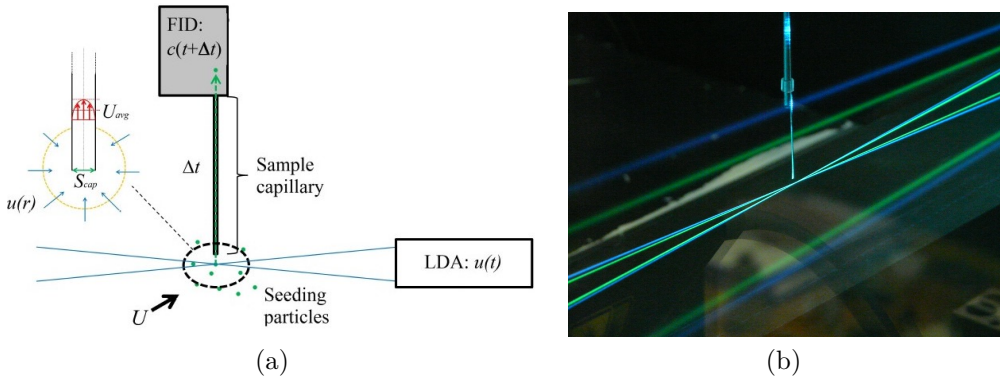

(a) (b)

Figure 2.8: *(a) Schematic representation of the FID-LDA system (Marro et al., 2020); (b) real coupled FID-LDA measurement.*

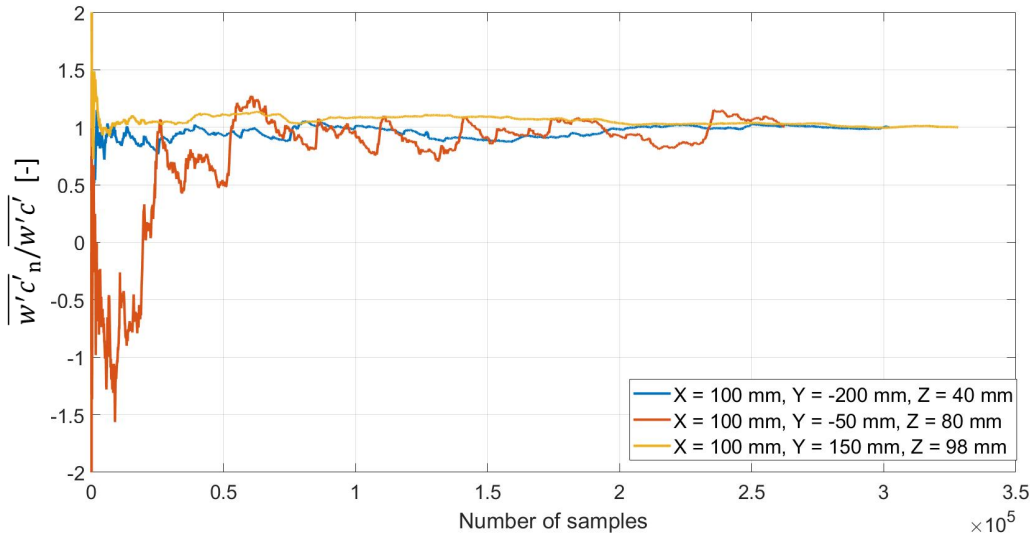

Figure 2.9: *Convergence of the mean of* $\overline{w'c'}$.

As explained above, LDA and FID operate with different working principles: the first one measures the velocity by lightening a particle through a laser beam, while the second one needs to displace the same particle towards the combustion chamber. As a consequence, the two measurements do not occur at the same time, but the concentration one is acquired a few milliseconds later, as the particle has to pass through the sampling tube and reach the flame chamber. The decoupling of the acquisition times leads to a shifting of the signal of concentration with respect to the velocity one, which has to be corrected in post-processing to obtain a reliable cross-correlation between them. Moreover, the FID has a constant sampling frequency while the LDA does not. Consequently, the two quantities have to be resampled on the same frequency, namely the LDA frequency. The technique employed to post-process the data is the sample-and-hold (S+H) method (Marro et al., 2020). Its goal is to find the time lag (Δt_{lag}) that provides the maximum correlation between the vertical velocity fluctuations ($w(t)$-$\overline{w}$) and the the concentration fluctuations ($c(t)$-$\overline{c}$). The S+H method develops in three steps:

- shifting the concentration time series of a certain Δt_{lag};
- resampling the concentration values on the temporal pattern of the velocity time series, applying the nearest neighbor interpolation method when the correspondence between velocity and concentration data is missing;
- computing cross-correlation weighted by the transit time.

The procedure reported above is applied using different time lags, in order to study the behavior of the correlation with respect to them. The curve presents a maximum, which identifies the time shift between the signals suitable to obtain the maximum correlation. The results of the iterative procedure, applied on one measurement point, are reported in figure 2.10. When the two time series are shifted, the tails of the concentration and velocity signals that do not overlap are eliminated. Therefore, the length of the coupled concentration-velocity signal decreases with the time lag.

Turbulent mass fluxes have been estimated on a central vertical section, using the same measurements grid defined for the velocity measurement campaign, and on a horizontal section at the rooftop of the canyon (Z=98 mm), measuring longitudinal profiles at X=50, 100, 150 mm.

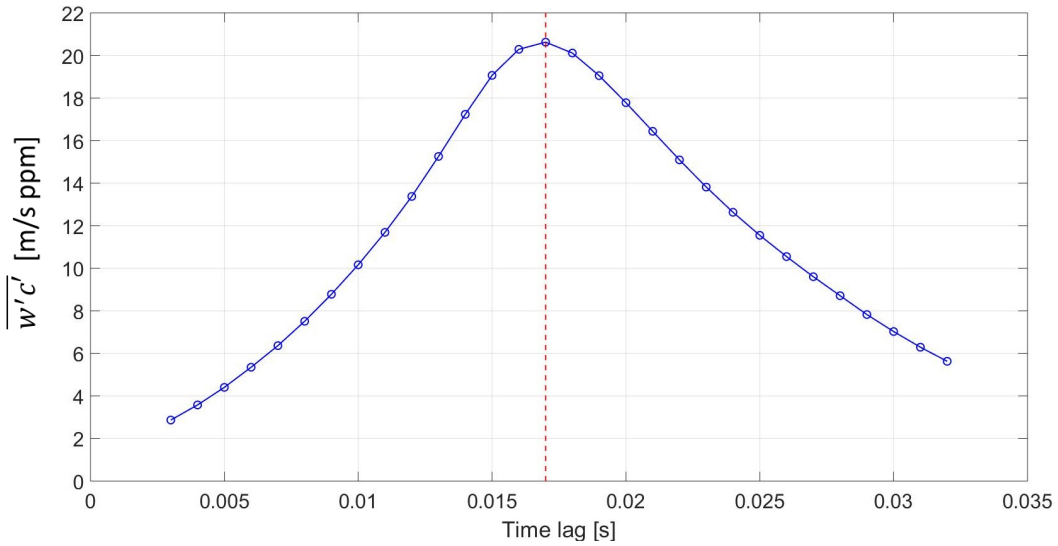

Figure 2.10: *Behavior of the correlation with respect to* Δt_{lag}.

Chapter 3

Results

In this chapter, the results of the experimental campaign will be presented. In Section 3.1, we will analyze quantities averaged over time, namely concentration, velocity and mass fluxes, while in Section 3.2 we will focus on time series of concentration and turbulent mass and momentum fluxes.

3.1 Flow and concentration fields

3.1.1 Concentration field

Concentration measurements have been acquired according to the grids reported in figure 2.5. Their high resolution provides a three-dimensional characterization of the concentration field inside the reference street canyon. The concentration will be expressed in the non-dimensional form $\overline{C}U_\infty \delta L_\mathrm{s}/Q_\mathrm{et}$, where $\overline{C}$ is the time averaged concentration, U_∞ is the velocity at the top of the boundary layer, δ is the boundary layer depth, L_s is the the source length and Q_et is the ethane flowrate. The results are organized in two-dimensional sections obtained from the interpolation of the concentration measured on the grid points.

In figure 3.1 transversal sections of mean concentration, extracted in the center of the cavity (around Y=0 mm) and in two symmetrical sides (at Y=-200 mm and Y=200 mm), are reported for the four configurations of tree density. Regardless of the presence of trees, a clear increase in the concentration from the downwind wall to the upwind wall can be observed in all sections. This pattern, which is in accordance with previous studies (Gromke and Ruck, 2007, 2009; De Giovanni, 2019; Balestrieri, 2021), highlights the action of the main recirculating cell: the fresh air enters the canyon at the downwind wall and transports the pollutant to the upwind wall, where part of it accumulates at the lower corner, part is moved outside and part is entrained towards the downwind wall. The recirculating structures are maintained in the different sections in the Zero and One-tree configurations, while increasing the

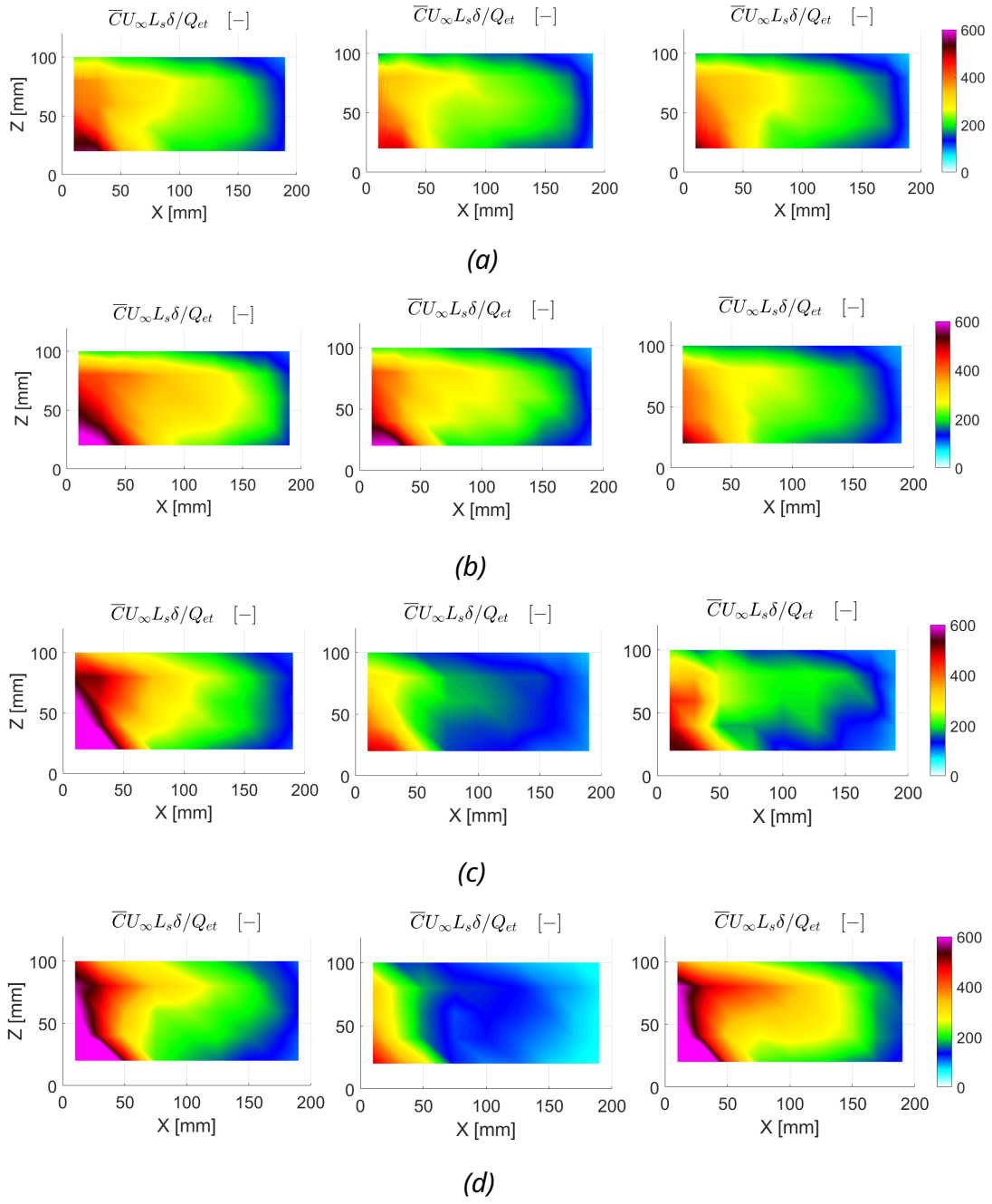

Figure 3.1: *Two-dimensional XZ sections of mean concentration at (a) Y=-200 mm, Y=0 mm, Y=200 mm (Zero configuration); (b) Y=-200 mm, Y=50 mm, Y=200 mm (One-tree configuration); (c) Y=-210 mm, Y=-30 mm, Y=210 mm (Half configuration); (d) Y=-215 mm, Y=0 mm, Y=215 mm (Full configuration).*

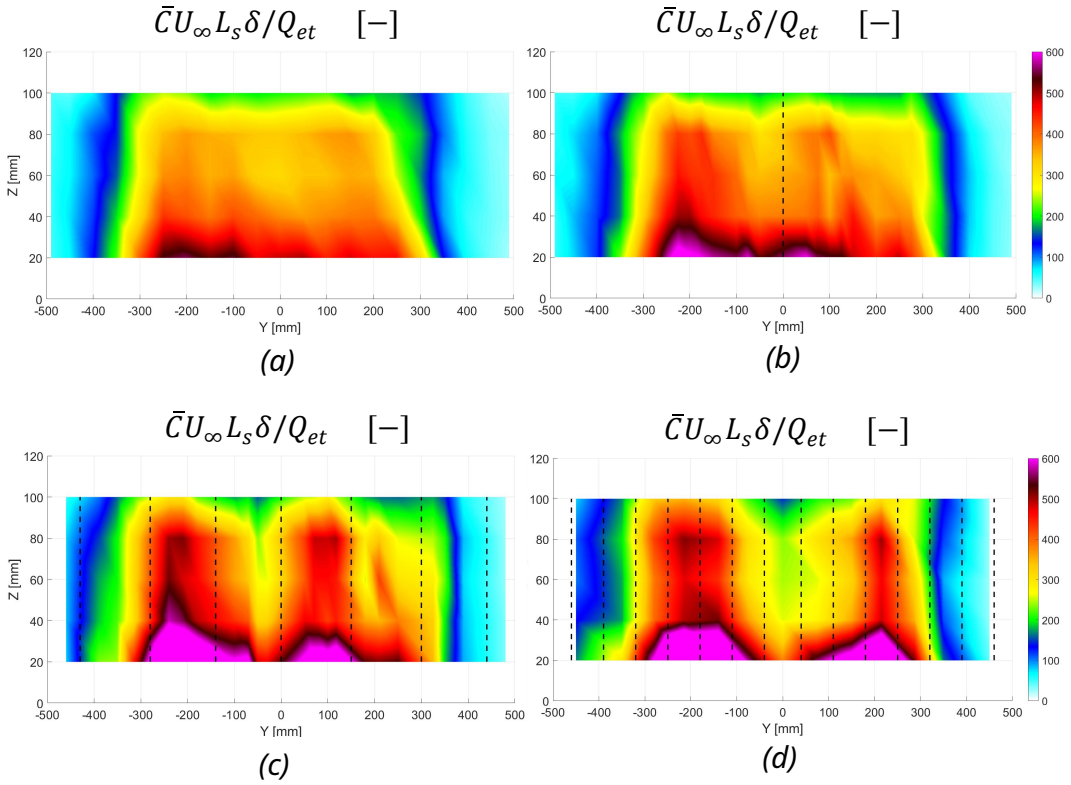

Figure 3.2: *Two-dimensional YZ sections of mean concentration at X=30 mm. (a) Zero configuration; (b) one-tree configuration; (c) half configuration; (d) full configuration. Trees are represented by the black dotted lines.*

tree density they are less defined. The recirculation seems to weaken mostly in the center of the canyon (central sections of figure 3.1c,d) where it is clear that, at the top of the canyon, the transport from the upwind wall back to the downwind wall is no more present, resulting in a lower concentration at the downwind wall with respect to the cases without trees or with a single tree. Moreover, we can notice a greater accumulation of pollutants at the upwind wall in the cases with trees. Therefore, looking at the different sections we have noticed that the concentration pattern is constant in the Zero and One-tree configurations, and the structure of the recirculating cells is perturbed when the number of trees is increased.

To better visualize the spatial inhomogeneity of the concentration field along the canyon, in figures 3.2-3.4 the concentration field is represented with longitudinal sections (YZ), extracted at three different positions: one close to the upwind wall (X=30 mm), one in the middle of the canyon (X=100 mm) and one close to the downwind wall (X=170 mm). It is confirmed that the presence of trees alters the homogeneity of the concentration field along the longitudinal direction of the

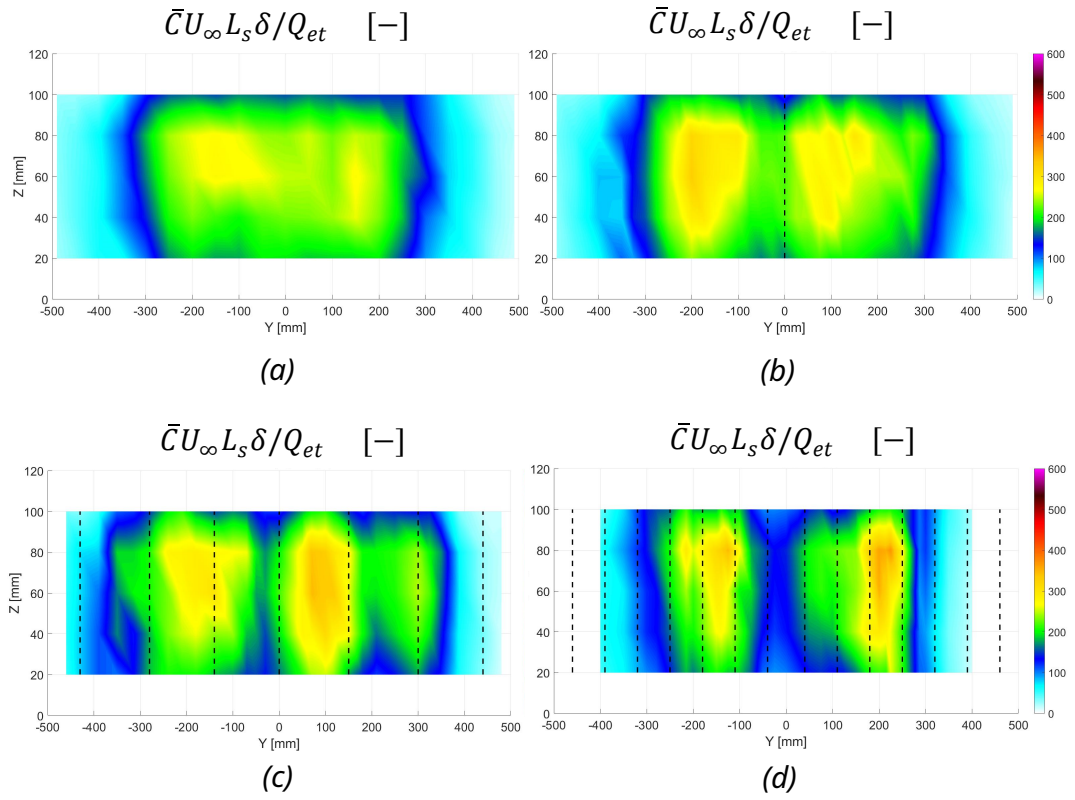

Figure 3.3: *Two-dimensional YZ sections of mean concentration at X=100 mm. (a) Zero configuration; (b) One-tree configuration; (c) Half configuration; (d) Full configuration. Trees are represented by the black dotted lines.*

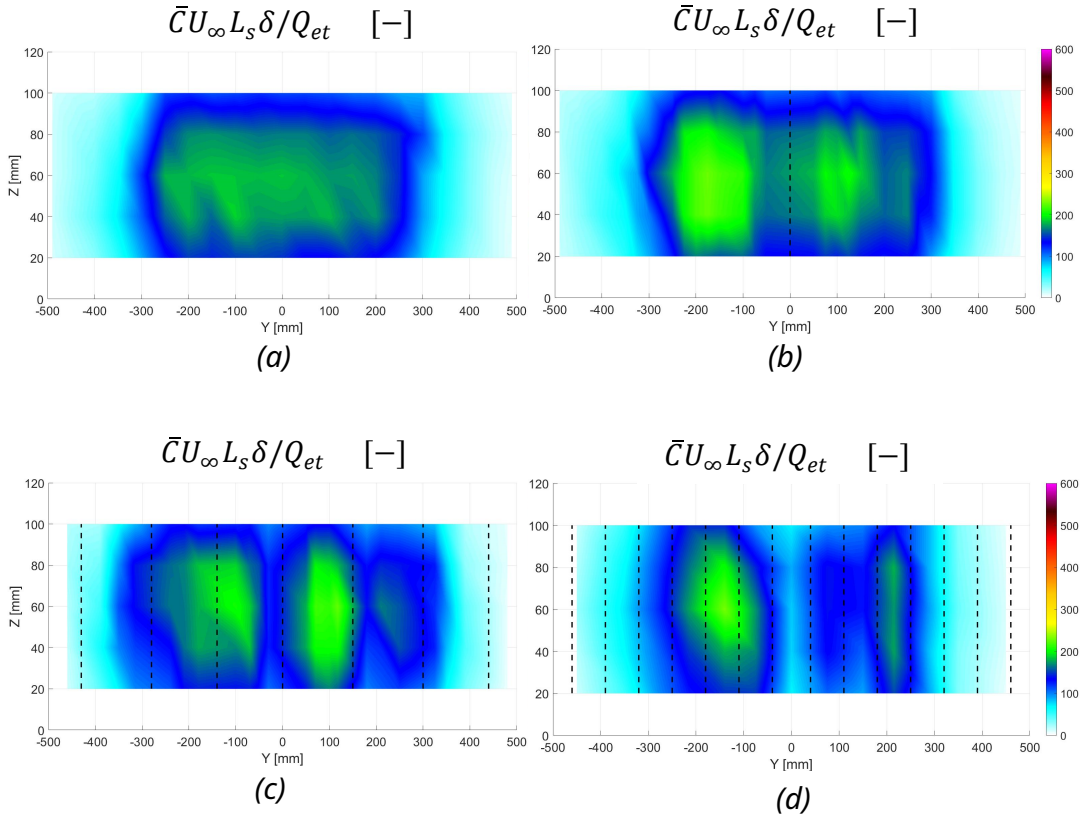

Figure 3.4: *Two-dimensional YZ sections of mean concentration at X=170 mm. (a) Zero configuration; (b) One-tree configuration; (c) Half configuration; (d) Full configuration. Trees are represented by the black dotted lines.*

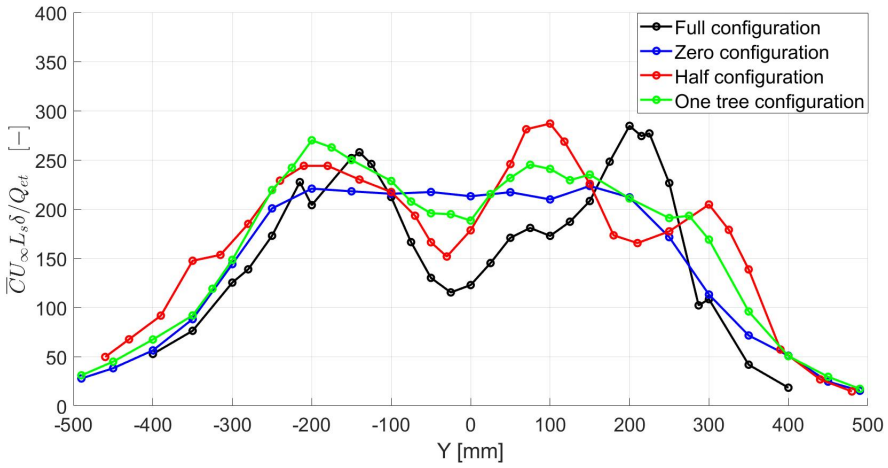

Figure 3.5: *Longitudinal mean concentration profiles averaged over Z, at X=100 mm.*

canyon. In particular, in the Full configuration it is possible to identify a lower concentration area in the middle of the canyon and two nearly symmetric accumulation areas at the sides. In the case with lower tree density, the concentration field is even more heterogeneous, as we can identify three accumulation areas separated by two lower concentration areas. Looking at the sections crossing the trees, at X=30 mm (close to the upwind wall), in figure 3.2, and at X=170 mm (close to the downwind wall), in figure 3.4, we can notice that the structure with peaks of the concentration field is preserved. The increase of concentration from the downwind wall to the upwind wall is still detectable: the concentration in the sections acquired at X=30 mm reaches higher maximum values compared to the ones of the sections acquired at X=170 mm. Notice that the low concentration values close to the edges are due to the fact that the ethane source does not cover the entire length of the canyon (see yellow line in figure 2.5).

By averaging the concentration over the vertical direction, we obtain the concentration profiles along the Y direction, at different transversal positions. The longitudinal profiles extracted in the middle of the canyon are reported in figure 3.5. It is clear the transition from a constant concentration behavior in the empty canyon to the structure with peaks in the vegetated canyon. Moreover, we observe that the increase in the number of trees produces a decrease in the minimum concentration. The difference between the structure of the profile of the Half configuration, characterized by three peaks, and the one of the Full configuration, characterized by two peaks, may be linked to the different arrangement of the trees. In particular, the main difference is the presence of a couple of trees in the center of the canyon (see figure 2.5c) in the Half configuration.

Finally, we analyze the concentration field on horizontal sections, at the pedestrian level (Z=20 mm. Figure 3.6) and close to the rooftop of the street canyon (Z=80 mm. Figure 3.7). The heterogeneity of the concentration field produced by the presence of trees is maintained also at different heights, as well as the transversal concentration gradient. The concentration at the upwind wall is higher in the Half and Full configurations (figures 3.6c,d and figures 3.7c,d), which demonstrates that trees hinder the rising up of the airflow, thus the vertical transport of the pollutant. Moreover, we can observe that, for all the configurations, the concentration is higher at the pedestrian level (close to the source) than at the rooftop. This vertical gradient is dangerous for citizens' health, as they are exposed to the highest level of concentration present in a street canyon. However, the air quality conditions improve moving to the downwind side of the street, when the wind direction is perpendicular to the canyon. In a canyon without vegetation, the concentration at the downwind wall is roughly 3 times lower than the one at the upwind wall, while in presence of trees this difference increases up to roughly 8 times on average. Therefore, we can say that tree avenues improve the air quality at the downwind wall (considering a wind direction perpendicular to the street axis), as they hinder the re-entrainment of pollutant from the upwind wall to the downwind wall.

In addition to the average concentration, we have analyzed the variation of the fluctuation intensity (i_c) in the canyon. It is defined as the ratio between the concentration standard deviation and the mean concentration ($\sigma_c/\overline{C}$). In figure 3.8, we report i_c profiles averaged over Z. Despite the spatial variation of the mean concentration within the canyon, and of the concentration standard deviation as well, i_c is almost constant (around 0.6) and it is not affected by the presence of trees. Its increase at the edges of the canyon can be neglected as it is due to the decrease of the concentration in that area, which is not reached by the source.

3.1.2 Vertical exchange velocity

The analysis of the spatial variation of the concentration in the transversal, longitudinal and vertical directions of the street canyon, shows that the presence of trees determines the transition from a two-dimensional concentration field (see the constant behavior along the longitudinal direction in the empty cavity case) to a clearly three-dimensional one. However, it is not yet clear if it hinders the pollutant outflow. By calculating the vertical exchange velocity (u_d), we evaluated the efficiency of the ventilation of the street canyon. Assuming perfect mixing within the canyon, we adopt the box model with one degree of freedom, with the assumption that, in steady state conditions, the mass transfer towards the external atmosphere is only governed by the u_d parameter (Salizzoni et al., 2009). The canyon is modeled as a closed box with uniform pollutant concentration, where the flowrate which enters the canyon (equal to the ethane flowrate) is equal to the one which leaves

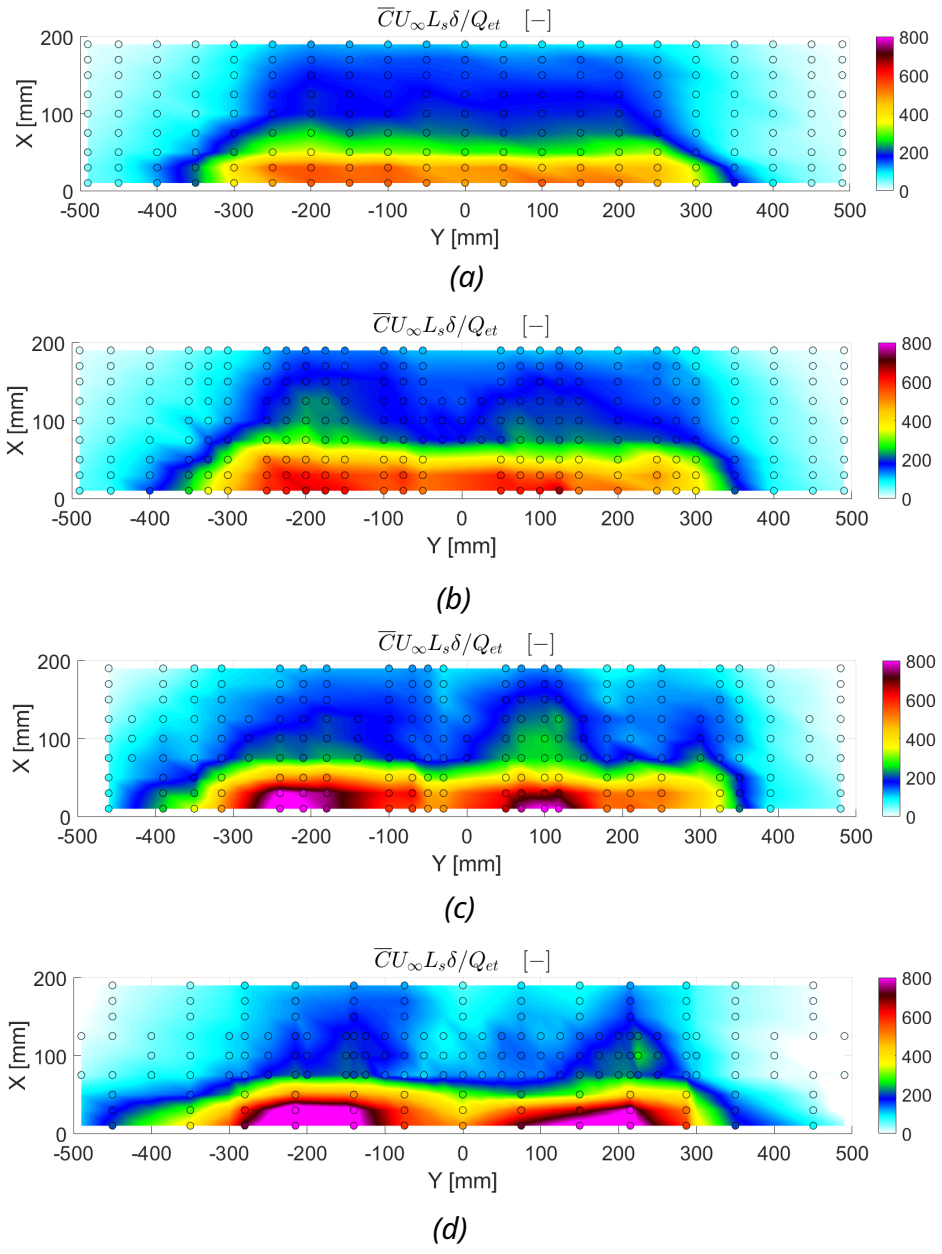

Figure 3.6: *Two-dimensional YX sections of mean concentration at Z=20 mm. (a) Zero configuration; (b) One-tree configuration; (c) Half configuration; (d) Full configuration. The small circules overlaid on the sections indicate the measurement grid.*

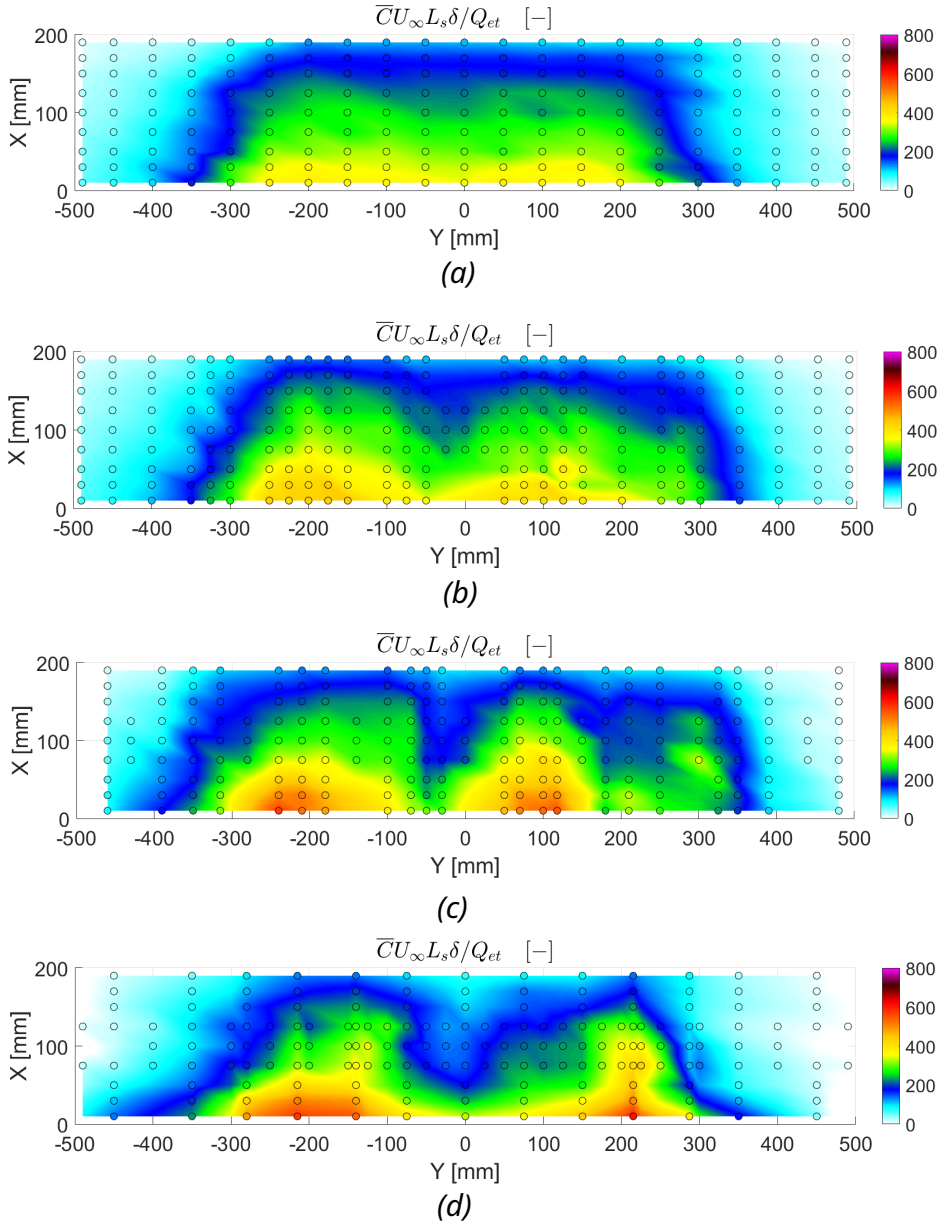

Figure 3.7: *Two-dimensional YX sections of mean concentration at Z=80 mm. (a) Zero configuration; (b) One-tree configuration; (c) Half configuration; (d) Full configuration. The small circules overlaid on the sections indicate the measurement grid.*

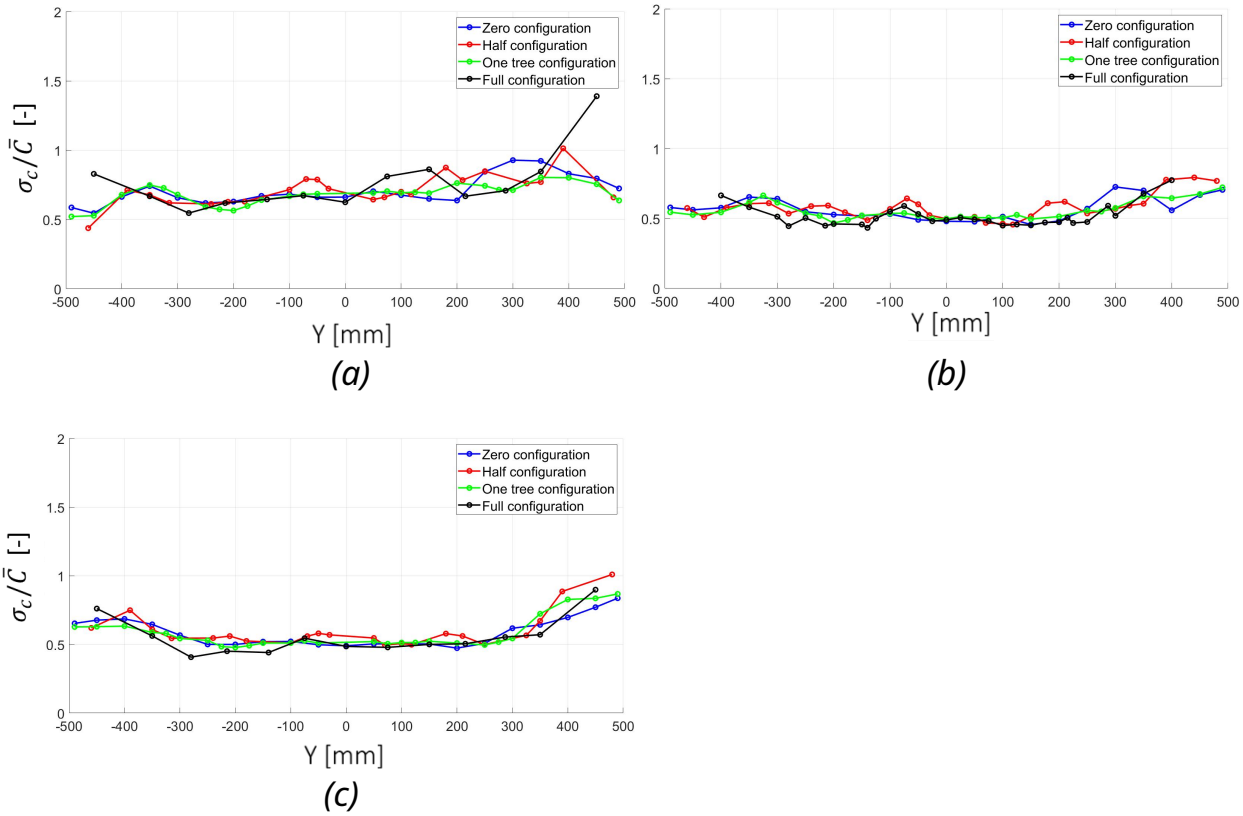

Figure 3.8: *Longitudinal profiles of fluctuation intensity averaged over Z at (a) X=30 mm; (b) X=100 mm; (c) X=170 mm.*

the canyon. The mass balance applied on the box can be written as:

$$q_{et} L_s = u_d C L W \tag{3.1}$$

where q_{et} is the ethane flowrate per unit of length at the source, L_s is the source length, u_d is the vertical exchange velocity, C is the average concentration calculated within the whole volume of the canyon, L is the length of the canyon and W is its width. By expressing the mean concentration in its non-dimensional form, u_d is obtained as:

$$\frac{u_d}{U_\infty} = \frac{L_s \delta}{C_* L W} \tag{3.2}$$

where C_* is the non-dimensional concentration averaged over the space. The u_d will be normalized by U_∞ and u_* (we recall that it is equal to 0.22 m/s) to do comparisons with other studies. The average concentration has been calulated applying different methods:

- rough mean of the non-dimensional concentration data (purple line in figure 3.9);
- mean of the non-dimensional concentration data interpolated on a regular grid, spaced 20 mm along X and Z directions and 50 mm along the Y direction (orange line in figure 3.9);
- mean of the non-dimensional concentration data, weighted by the distance between transversal sections, called dy (green line in figure 3.9);
- mean of the non-dimensional concentration data, weighted by dy and by the width of the transversal sections, called dx (yellow line in figure 3.9).

It was interesting to analyze the influence of the weighting factors, dy and dx, because in presence of trees the spacing and the width of the transversal measurement sections are not constant (see the vertical dotted lines in figure 2.5), thus the rough mean calculated according to the first method could be influenced by the number and position of the measurement points. The irregular spacing is due to the fact that more measurement sections have been acquired to define the shape of the peaks of the profiles, while narrower widths were necessary between trees.

The obtained u_d, normalized by U_∞ and u_*, are reported in figure 3.9. We can observe that the weighting factors applied to the mean concentration cause the greatest difference between the u_d values in the Full configuration. This is due to the fact that the acquisition grid used in the Full configuration is more irregular. However, this difference is almost 2%, thus we can state that the inhomogeneity of the grid of acquisition does not influence significantly the evaluation of the mean concentration. Looking at the variation of the u_d, calculated considering the interpolated mean concentration (orange line in figure 3.9), we can notice that it

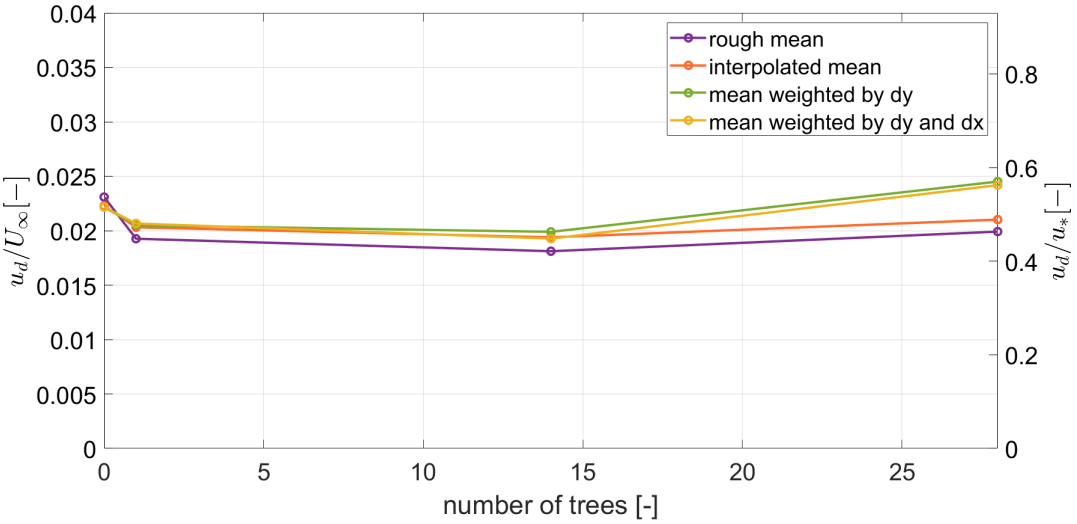

Figure 3.9: *Variation of u_d with respect ot the number of trees. Different colors are referred to the different methods used to calculated C_*.*

is almost constant with the increase of the number of trees. This highlights that the presence of trees induces the spatial variation of the concentration field, but it does not influence the vertical exchange velocity. This result is not in line with Balestrieri (2021) (see table 3.1), who found that the presence of trees decreases the ventilation efficiency. However, it should be noticed that in the previous experimental campaign the u_d has been calculated over a small control volume, in the center of the cavity (namely, at -100 mm<Y<100 mm) which, in the Full configuration, includes the two peaks of concentration and the minimum. For this reason, the peak concentration has a higher contribution to the overall mean, which results

Table 3.1: *Comparison between the u_d obtained in the present study and the ones retrived in previous experimental campains.*

	Balestrieri (2021) (H/W = 0.5)		**Mechinaud, Barulli, Del Ponte (H/W = 0.5)**			
	No trees	**14 trees**	**No trees**	**1 tree**	**7 trees**	**14 trees**
$\frac{u_d}{U_\infty}$	0.026	0.023	0.022	0.020	0.019	0.021
$\frac{u_d}{u_*}$	0.60	0.53	0.52	0.47	0.45	0.49
	Salizzoni (2006)		**Fellini et al. (2020) (H/W = 1)**			
	H/W = 0.5	**H/W = 1**	**Δ T = 0 K**	**ΔT = 70 K**	**ΔT = 170 K**	
$\frac{u_d}{U_\infty}$	0.015	0.013	0.01	0.02	0.017	
$\frac{u_d}{u_*}$	0.23	0.20	0.22	0.33	0.35	

higher than in the present study, and therefore provides a lower u_d.

The u_d is also compared with other experimental studies which focused on other factors affecting the canyon ventilation. Salizzoni (2006) has found that the u_d decreases with the increases of the aspect ratio (H/W), as the narrowing of the canyon hinders the air circulation. Fellini et al. (2020) found that if the downwind wall of the canyon is heated the vertical exchange is enhanced. The u_d found in the present work is higher than the one found by Fellini et al. (2020), as the canyon is wider. Considering the same aspect ratio, the u_d found by Salizzoni (2006) is lower than the one found in this study, probably due to a different method involved in its estimation (they estimated u_d considering a box model with two degrees of freedom used to describe the canyon washout), and a different experimental setup.

3.1.3 Velocity field

So far, we know that the presence of trees induces the transition from a two-dimensional concentration field to a three-dimensional one. We want to investigate how the velocity field modifies among Zero, Half and Full configurations. For this purpose, the velocity field has been measured on a longitudinal section located in the center of the canyon (X=100 mm). The number of measurements points along the longitudinal direction of the canyon has been established by observing the behavior of the concentration profiles: points 50 mm apart for the Zero configuration, as the concentration is constant, and a more refined spacing, depending on the shape of the concentration profiles, for the Half and Full configurations.

The characterization of the mean flow is reported in figure 3.10. Looking at the mean velocity component along the wind direction ($\overline{U}$), a homogeneous recirculating structure can be identified in all configurations: $\overline{U}$ is positive at the top of the canyon, where the external flow goes towards the downwind wall, and it is negative at the bottom of the canyon, where the flow is diverted towards the upwind wall. The mean longitudinal velocity component ($\overline{V}$) is quite homogeneous in the different configurations and shows values around zero. This result reveals that the flow field inside the canyon is basically two-dimensional. However, we notice that there is a spatial variation of positive and negative values of $\overline{V}$ that forms zones of convergence: they are distributed mostly on the side where the Y coordinate assumes negative values in the Zero and Full configurations, while in the Half configuration they are distributed everywhere. The vertical component of the mean velocity ($\overline{W}$) presents a heterogeneous structure in the Zero configuration, with two symmetric zones of positive velocity values (at Y=-150 mm and Y=+150 mm), and three zones of negative velocity values at the edges and in the center of the canyon. On the contrary, the vertical mean velocity field is homogenized in the Full configuration. The spatial inhomogeneity of $\overline{W}$ in the Zero configuration and its spatial homogeneity in the Full configuration are quite unexpected having in mind

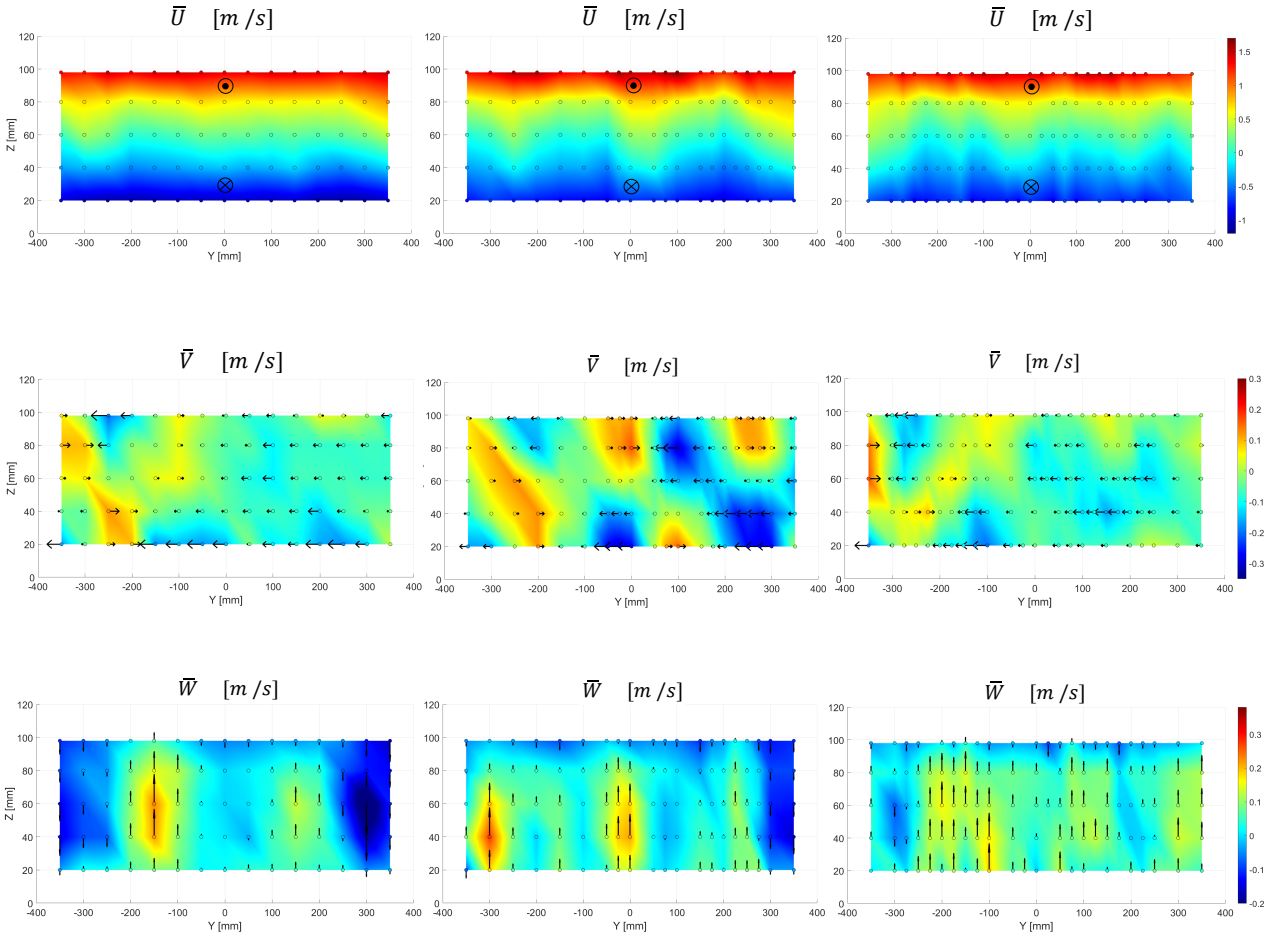

Figure 3.10: *YZ sections of the three mean velocity components at X = 100 mm. Zero configuration on the left, Half configuration in the center, Full configuration on the right.*

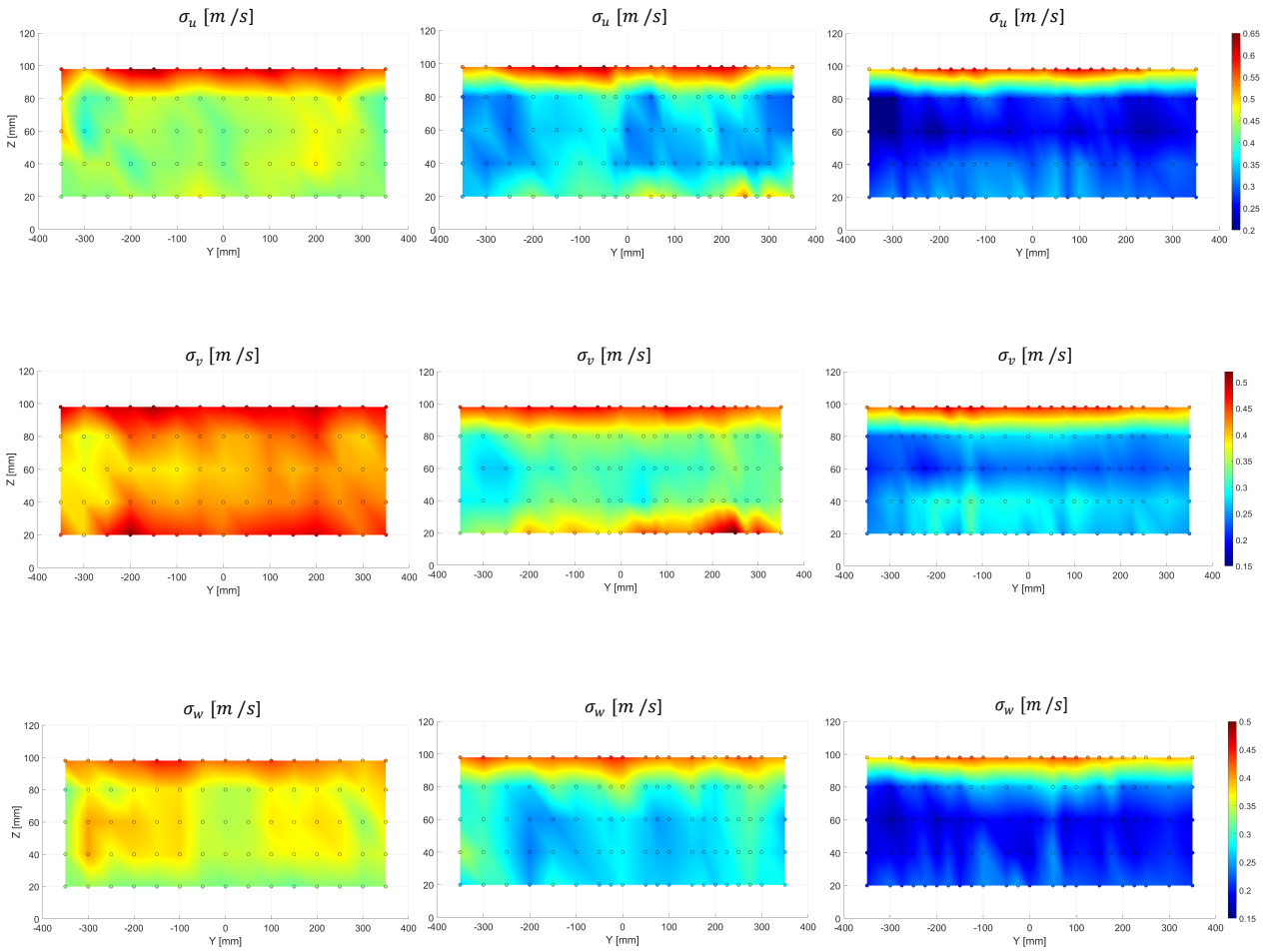

Figure 3.11: *YZ sections of the three fluctuating velocity components at X=100 mm. Zero configuration on the left, Half configuration in the center, Full configuration on the right.*

that the concentration field behaves in the opposite way (it is homogeneous in the Zero configuration and it presents to peaks in the Full configuration). However, we have to consider that the sections where we have measured the vertical velocity is not rappresentative, as it is in the center of the canyon where the vertical velocity is very low. We expect that close to the walls, where the vertical velocity is different from zero, the hindering effect of trees is more detectable.

The three fluctuating components of the velocity are reported in figure 3.11. Knowing them we can calculate the turbulence kinetic energy (TKE):

$$TKE = \frac{1}{2}(\sigma_u^2 + \sigma_v^2 + \sigma_w^2) \tag{3.3}$$

which is reported in figure 3.12. Looking at the results, we can identify a shear

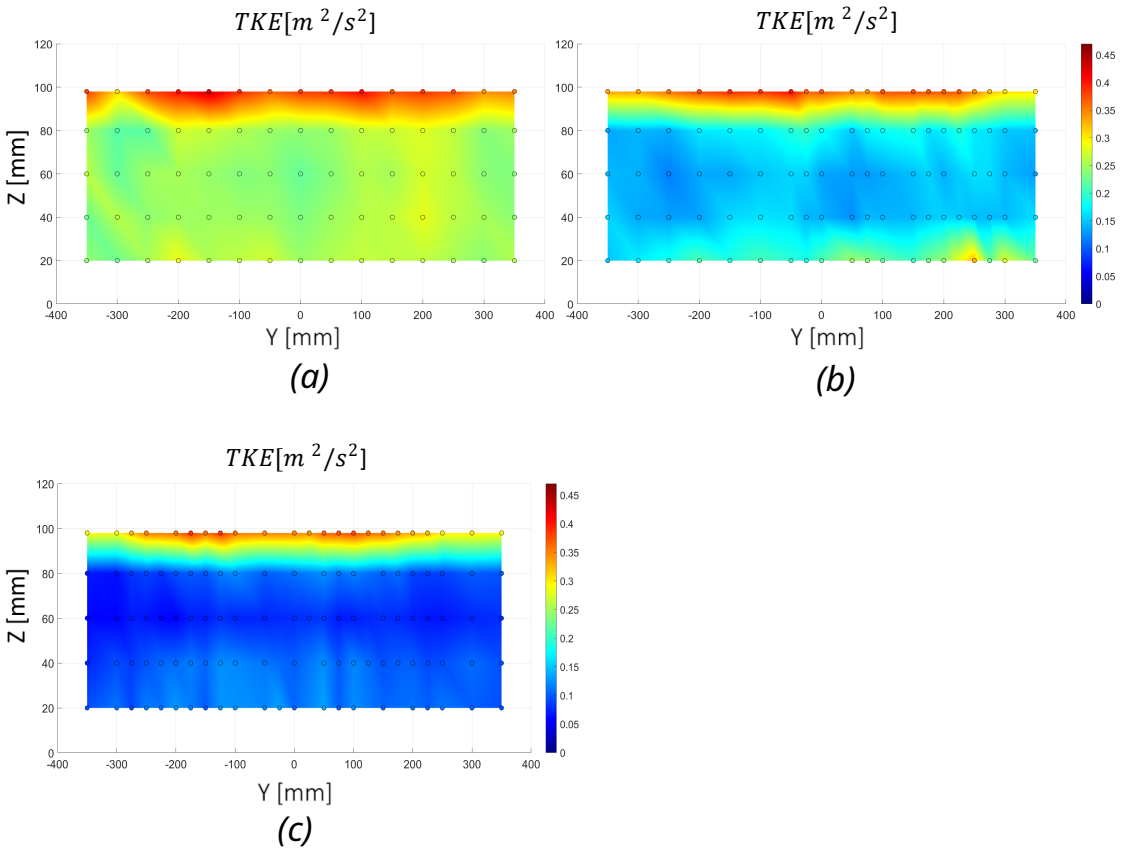

Figure 3.12: *YZ sections of TKE at X=100 mm. (a) Zero configuration on the left; (b) Half configuration in the center; (c) Full configuration on the right.*

layer of almost two centimeters at the rooftop of the canyon, where both the TKE and the velocity fluctuations show a sharp increase. This happens because at the interface between the canyon and the external atmosphere the turbulence is very high, as it is the zone where there is the interaction between the external flow and the canyon flow. Outside the shear layer, inward of the cavity, the TKE decreases and it is distributed homogeneously (Salizzoni et al., 2011). Velocity fluctuations decrease as well inside the canyon, except for the lateral velocity fluctuations (σ_v), that in the Zero configuration is high and homogeneous in the whole canyon (see the σ_v section on the left side of figure 3.11). It may identify the presence of lateral mixing, which suggests a homogenization of the concentration field.

Comparing the TKE among the different configurations, we notice that it decreases gradually with the increase of the density of the trees. The same result has been obtained for all the fluctuating components of the velocity field. Fellini et al. (2020) reports that for a squared canyon ($H/W = 1$) the decrease of the TKE led to a decrease in the ventilation efficiency of the canyon, thus it is linked to a

decrease in the u_d, which we do not observe in this study. The reason may lie in the fact that the different canyon widths cause different flow regimes. Indeed, when $H/W = 1$ the *skimming flow regime* governs the air circulation inside the canyon (figure 1.2a). It expects the formation of a close recirculating structure inside the canyon, which does not interact with the external atmospheric flow. Therefore, in that configuration, the turbulent fluctuations are essential to transfer the pollutant through the streamlines of the mean recirculating flow, towards the shear layer, and, in this sense, they are responsible for the ventilation of the canyon. On the contrary, in the canyon subject of this study (where $H/W = 0.5$), the mean flow dominates the ventilation, thus the decrease in the TKE does not decrease the u_d.

3.1.4 Vertical mass fluxes

Finally, we are interested in evaluating the vertical mass fluxes both at the rooftop and inside the canyon. The transport of a passive scalar in a turbulent flow is described by the Reynolds-averaged advection-diffusion equation. Neglecting molecular diffusion and assuming stationary conditions, the total vertical mass transport within the canyon can be expressed as the sum of a convective component ($\bar{w}\bar{c}$) and a turbulent component ($\overline{w'c'}$). The former is the product between the mean vertical velocity and the mean concentration, while the latter is the mean of the correlation between velocity and concentration fluctuations. Concentration fluctuations (c') and velocity fluctuations (w') are respectively expressed as $c(t)$ - $\overline{c}$ and $w(t)$ - $\overline{w}$, where $c(t)$ and $w(t)$ are the instantaneous concentration and velocity values and $\overline{c}$ and $\overline{w}$ the respective means. To evaluate turbulent mass fluxes, velocity and concentration measurements have been acquired simultaneously, applying the procedure illustrated in section 3.2.4. The aim of this investigation is to understand if the spatial evolution of the concentration is dominated by the turbulent component of the vertical mass flux or the convective one. Quantities will be reported in the non-dimensional form: $(\overline{c},\, c')U_\infty \delta L_\mathrm{s}/Q_\mathrm{et}$ and $(\overline{w},\, w')/U_\infty$.

Figure 3.13 shows mean, turbulent and total vertical mass fluxes measured at the rooftop of the canyon (Z=98 mm). In the empty canyon case, there is a homogeneous negative mean mass flux close to the downwind wall (X=150 mm), which indicates clean air that enters the canyon, and a homogeneous positive mean mass flux at the upwind wall (X=50 mm), which indicates polluted air that leaves the canyon. This pattern is found in the vegetated canyon cases as well, but it is more heterogeneous as the vertical mass fluxes are hindered by the trees. Considering the different tree densities, it seems that the positive mean vertical flux is lower in the Half configuration. The turbulent mass fluxes (figure 3.13b) are always positive, and, towards the upwind wall, they are stronger in presence of trees. It means that, in presence of trees, turbulent fluxes enhance the vertical transport of polluted air outside the canyon at the upwind wall, where the mean fluxes are blocked, thus the

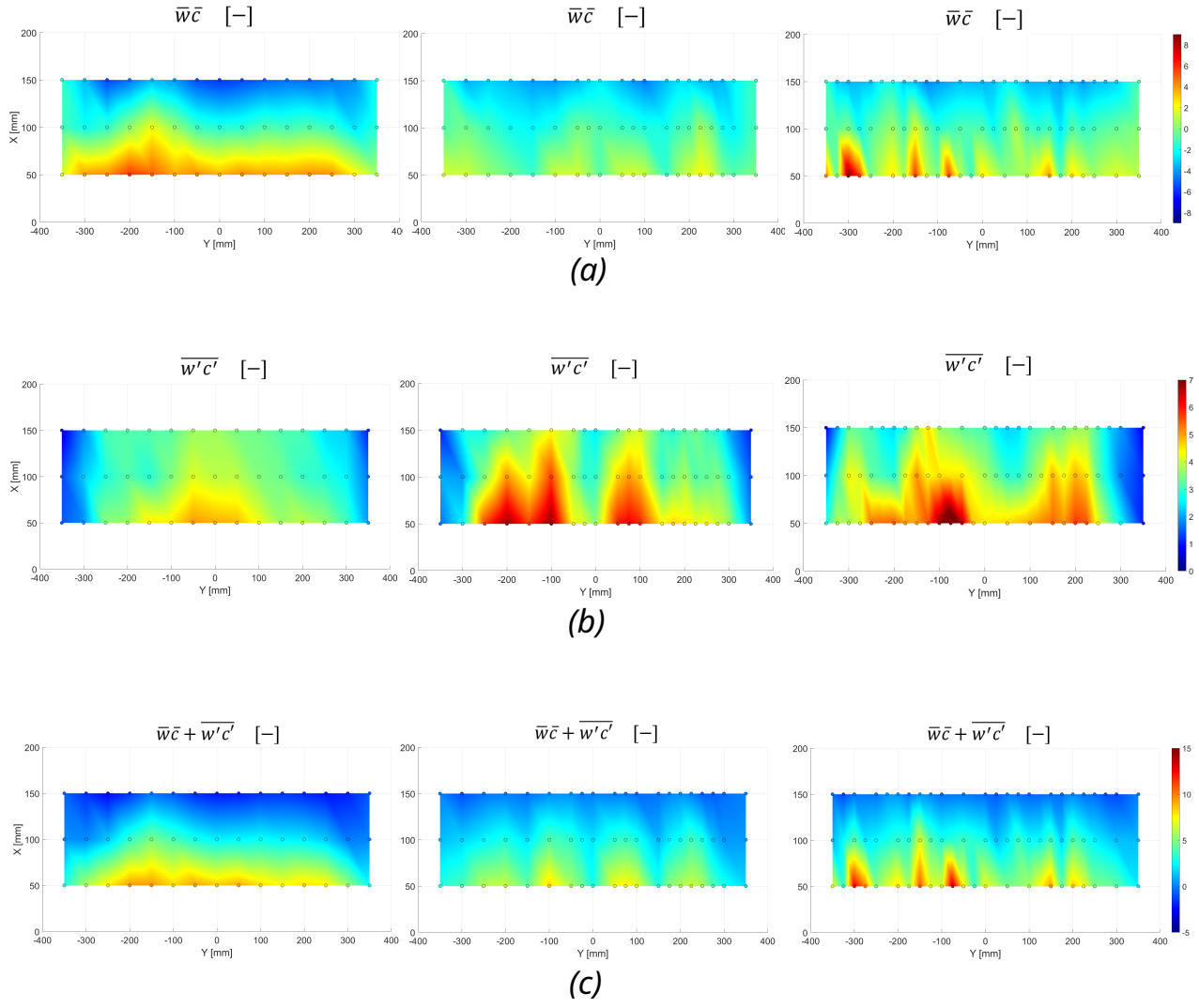

Figure 3.13: *Horizontal section at the rooftop (Z=98 mm) of vertical mass fluxes in Zero configuration (left), Half configuration (center) and Full configuration (right). (a) Mean vertical mass fluxes; (b) turbulent vertical mass fluxes; (c) total vertical mass fluxes.*

ventilation efficiency does not result lower than the one in the empty canyon case. Looking at the total mass fluxes (figure 3.13c), the same recirculating structure (incoming flow at the downwind wall and exiting flow at the upwind wall) found in the mean flow, as well as the spatial behavior, can be identified in all the three configurations, thus we can say that the convective component dominates the vertical mass flux at the rooftop.

The total and the mean vertical mass fluxes measured inside the canyon (figure 3.14c, 3.14a) follow the same spatial behavior of the mean vertical velocity ($\overline{w}$, figure 3.10), with well defined cells in the Zero configuration and homogeneous structure in Half and Full configurations. Indeed, in the Zero configuration we can identify three cells of negative mean fluxes, namely negative incoming fresh air, and two cells of positive mean fluxes, namely positive outgoing polluted air. The increase of the turbulent mass fluxes at the rooftop (figure 3.14b), with respect to the ones detected inside the canyon, confirms that turbulence plays a key role in the vertical transport of pollutants in correspondence to the shear layer (Marucci and Carpentieri, 2019; Di Bernardino et al., 2018). Inside the empty cavity, turbulent mass fluxes are strongly negative, while in presence of trees they are close to zero. Comparing this result with the concentration profiles, we can hypothesize that the strong negative turbulent component homogenizes the concentration, but does not promote the transport of the pollutant outside, therefore the bulk vertical exchange velocity results the same with and without trees. This result denotes that the turbulent component of the mass flux influences the concentration field, even if the total vertical transport inside the canyon is controlled by the mean velocity field (Marucci and Carpentieri, 2019).

To understand if the ventilation of the canyon is governed by the entrance of clean air or by the leaving of polluted air, a quadrant analysis of the turbulent mass fluxes at the rooftop is performed (only Zero and Full configurations are considered). It is implemented by plotting on cartesian axes instantaneous values of concentration fluctuations ($c'(t)$) versus instantaneous values of vertical velocities fluctuations ($w'(t)$), both in their non-dimensional form. We obtain a point cloud that can be decomposed into four quadrants according to the sign of the two quantities:

- quadrant I: $c' > 0$, $w' > 0$. It indicates exiting flow with concentration greater than the mean (exiting polluted flow);
- quadrant II: $c' < 0$, $w' > 0$. It indicates exiting flow with concentration lower than the mean (exiting clean flow);
- quadrant III: $c' < 0$, $w' < 0$. It indicates entering flow with concentration lower than the mean (entering clean flow);
- quadrant IV: $c' > 0$, $w' < 0$. It indicates entering flow with concentration higher than the mean (entering polluted flow).

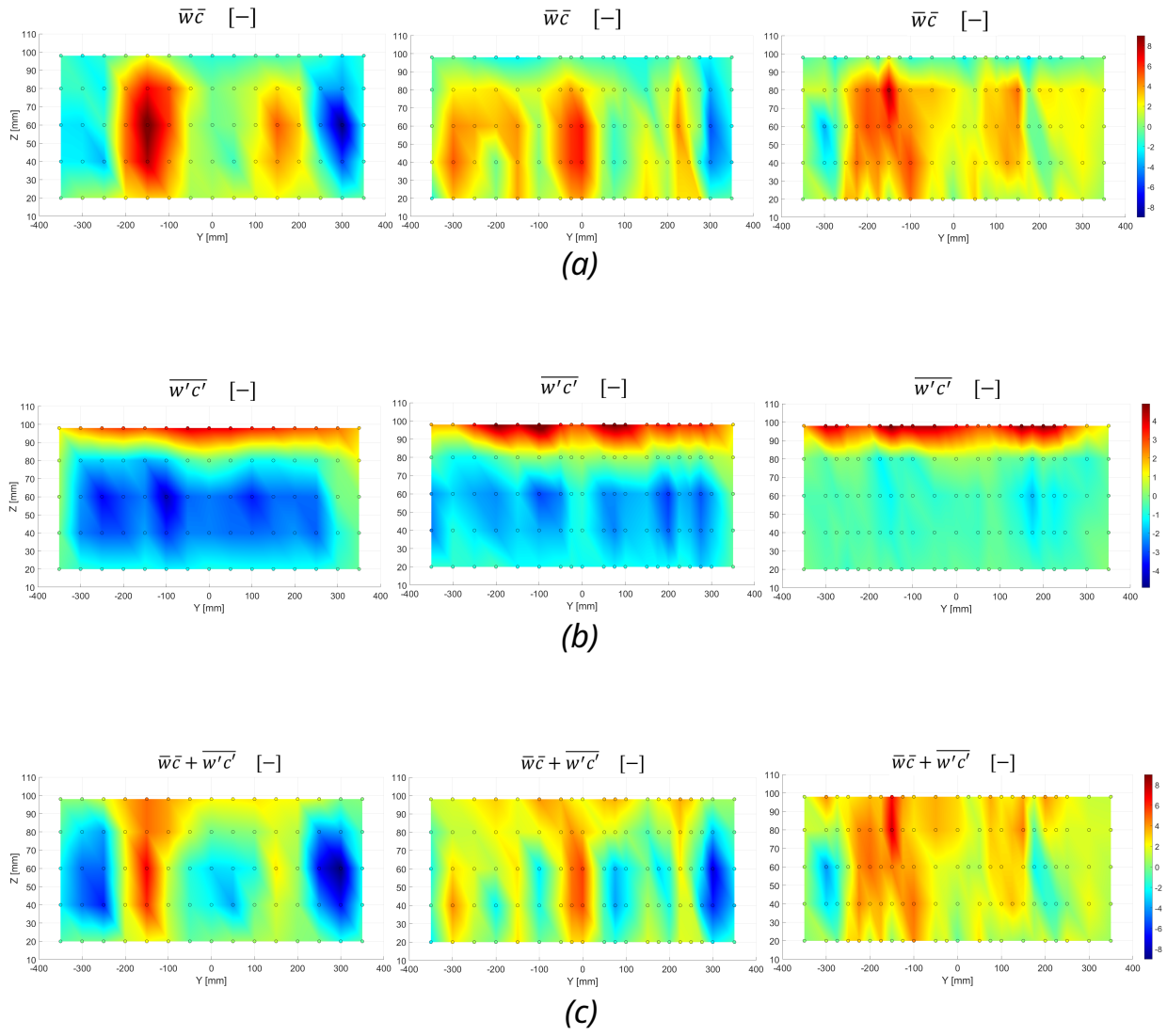

Figure 3.14: *Vertical section at X = 100 mm of vertical mass fluxes in Zero configuration (left), Half configuration (center) and Full configuration (right). (a) Mean vertical mass fluxes; (b) turbulent vertical mass fluxes; (c) total vertical mass fluxes.*

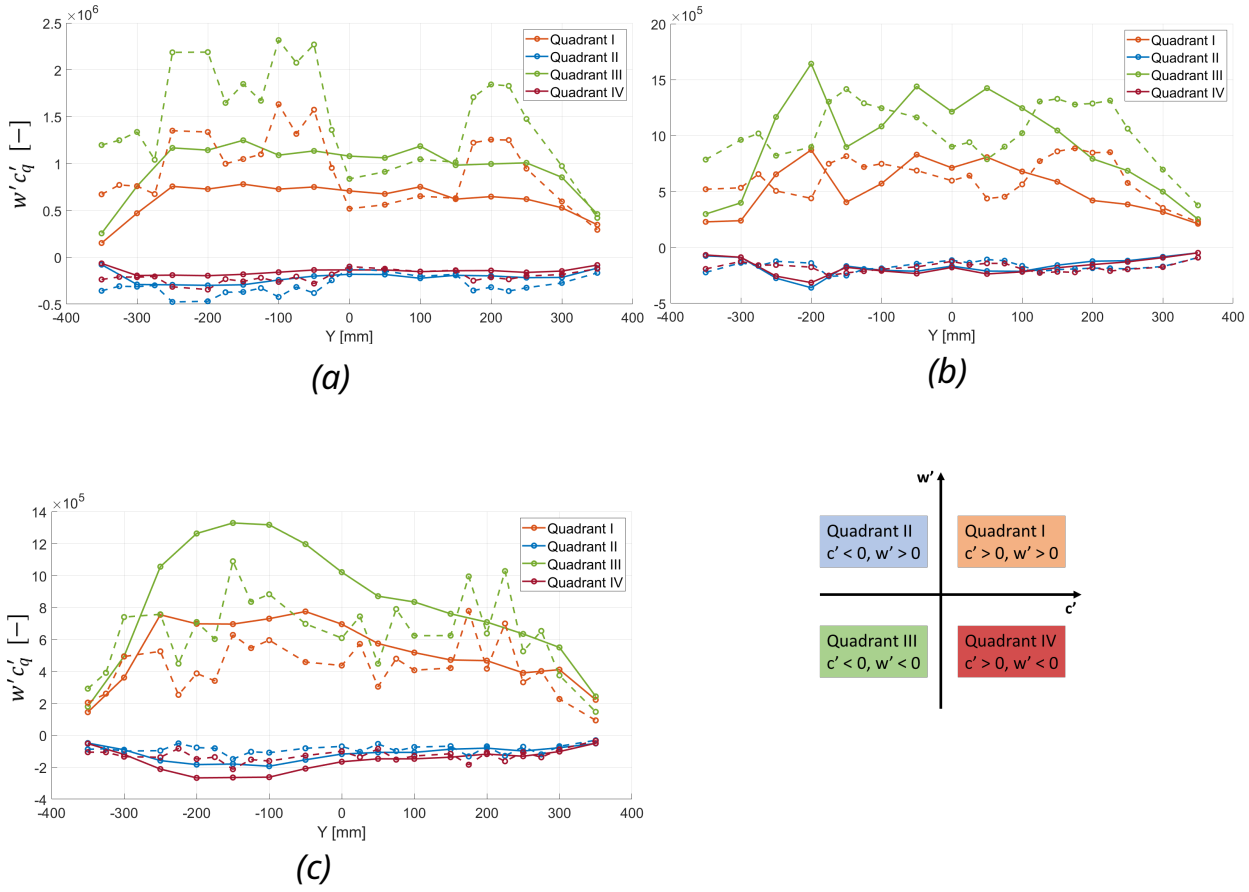

Figure 3.15: *Quadrant analysis of turbulent fluxes at the rooftop at (a) X=50 mm, (b) X=100 mm, (c) X=150 mm. Continuous lines indicate Zero configuration, dotted lines indicate Full configuration.*

The positive contributions to the air quality of the canyon are the ones of the I and III quadrants.

The contributions, to the vertical turbulent mass transfer, of the different types of air exchange mentioned above have been evaluated by plotting four profiles: each profile is the sum of the turbulent fluxes ($w'c'_q$, where $q = I, II, III, IV$) which belong to each quadrant (figure 3.15). The contributions of quadrants II and IV are negligible with respect to the ones of quadrants I and III. Both with and without trees, the vertical exchange at the rooftop is dominated by the entrance of clean air (quadrant III), rather than the leaving of polluted air (quadrant I). This result is in accordance with Marucci and Carpentieri (2019). Looking at the profiles of quadrants I and III close to the walls, above the rows of trees (figure 3.15a,c), we notice a clear distinction between the spatial homogeneity of the contributions of quadrant I and III in the Zero configuration and the inhomogeneity of them in the

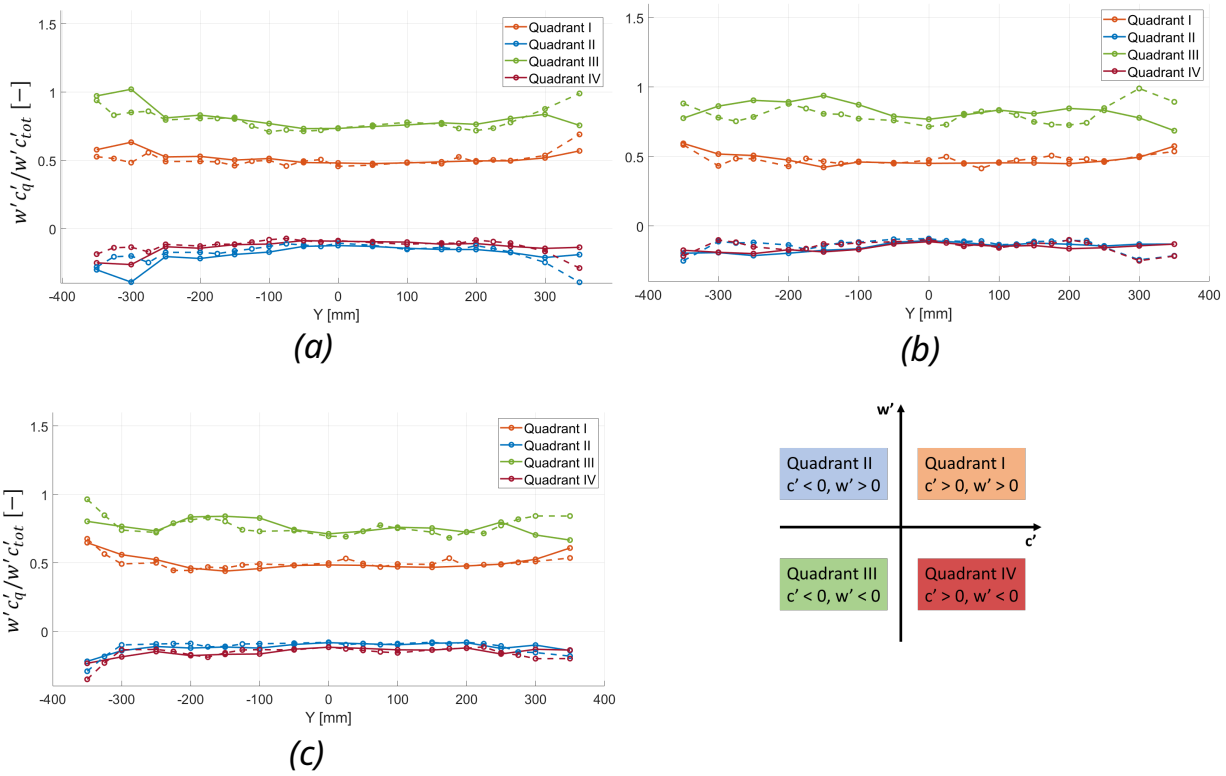

Figure 3.16: *Normalized turbulent fluxes. (a) X = 50 mm, (b) X = 100 mm, (c) X = 150 mm. Continuous lines indicate Zero configuration, dotted lines indicate Full configuration.*

Full configuration.

In figure 3.16, we report the turbulent fluxes of each quadrant ($w'c'_q$) normalized by the sum of the turbulent fluxes belonging to all quadrants ($w'c'_{tot}$). We notice that the contribution of each quadrant with respect to the sum of the contributions of all quadrants is equal in the space, and it is independent of the tree density. Therefore, moving to different points of the canyon the air exchange is governed by clean air that enters, but its contribution with respect to the total turbulent flux of all quadrants does not show zones where it is more significant than others. We can say that the contribution of each quadrant, to the vertical turbulent mass transfer, is equally divided in the whole canyon.

3.2 Time series analysis

In this section, we will work on the analysis of concentration, mass flux and momentum flux time series. In particular, we will analyze the spatial variability of

the Probability Density Function (PDF) of instantaneous concentration data, the autocorrelation of the concentration time series, and the power spectral density of mass and momentum turbulent fluxes.

3.2.1 Probability Density Function of the instantaneous concentration

The statistical characterization of concentration fluctuations has several applications, among these the assessment of health hazards due to the chronic exposure at high level of pollutant substances or the odors assessment. Due to their environmental utility, concentration PDFs of dispersing contaminated plumes have been deeply studied. As a consequence, a number of models have been proposed for fitting them, such as the Lognormal distribution, the Gamma distribution and the two-parameters Weibull distribution (Weibull 2p). Orsi et al. (2021) performed Direct Numerical Simulations (DNS) to model diffusion and mixing properties of a plume of passive scalar released in a homogeneous isotropic boundary layer. They report that the Gamma distribution is a suitable model to describe both the meandering phase and the dispersion phase, as it changes shape according to the fluctuation intensity parameter (i_c). It presents an exponential-like shape during the meandering phase (when i_c>1, as the signal is highly intermittent), it evolves into a Lognormal-like shape when the concentration starts to homogenize in the domain and into a Gaussian-like shape during the dispersion process (when i_c<1, as the intermittency is reduced). For modeling the phenomenon, Orsi et al. (2021) also studied the Lognormal distribution and the Weibull 2p distribution, and they found that the first one cannot reproduce the effects of the meandering process, while the second one is not suitable to describe the dispersion process. Nironi et al. (2015) presented the same result from the experimental point of view, performing wind tunnel experiments on the dispersion of a passive scalar emitted by a point source within a turbulent boundary layer. By analyzing concentration PDFs at various distances from the source they found again that the Gamma distribution fits both the exponential-like shape of the experimental PDF obtained near to the source, where the meandering motion dominates, and the Gaussian-like shape of the PDF obtained in the far field, where the dispersion dominates. F Yassin (2008) performed a statistical study on the dispersion of a plume in a boundary layer simulated in an open circuit wind tunnel. He found that the PDF of the concentration fluctuations is modeled by a lognormal distribution. Oettl and Ferrero (2017) reported that the Weibull 2p is a suitable model for odors assessment as it provides an analytical expression to calculate the 90^{th} percentile of the concentration, which provides results in good agreement with experimental observations.

In the present work, we will characterize the dispersion of the ethane, which behaves as a passive scalar, released by the linear source inside the reference street

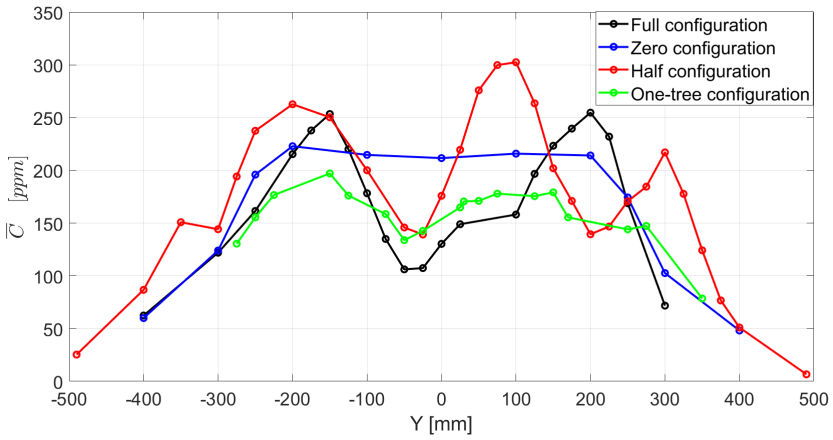

Figure 3.17: *Mean concentration profiles acquired at X=100 mm, Z=40 mm, with an acquisition time window of 300 s.*

canyon. The dataset involved has been constructed by collecting instantaneous concentration measurements ($c(t)$) in different spatial points organized on longitudinal profiles, represented in figure 3.17, acquired in the center of the street canyon (X=100 mm, Z=40 mm). One profile for each configuration is available. The acquisition time window of the FID has been set at 300 s, to collect time series of 300 000 concentration values in each point of the profiles. The acquired concentration values are cleaned by the background noise, but not averaged in time.

In order to identify the statistical model that better describes the dispersion phenomenon inside the canyon, the PDF from the experimental data has been estimated, from the instantaneous concentration data acquired in each point of the four longitudinal profiles reported in figure 3.17. The instantaneous concentration datasets were discretized in 100 classes of uniform width to construct the histogram. For each class, the corresponding PDF was estimated as:

$$pdf_i = \frac{counts_i}{\sum_{i=1}^{N} counts_i} \cdot \frac{1}{dx} \tag{3.4}$$

where i represents the classes, $counts$ is the number of samples in each class, N is the total number of classes and dx is the width of the classes. The ratio between the number of samples in each class and the total number of samples is called frequency distribution. It was verified that the total area under the estimated pdf_i is equal to 1, knowing the property:

$$\sum_{i=1}^{N} pdf_i \cdot dx = 1. \tag{3.5}$$

To compare the PDFs (both among different spatial points on the same profile, and among different profiles), and to constrain them starting from the origin of the

axis, the instantaneous concentration data are reported in the non-dimensional form $(c(t)\text{-}C_{min})/\overline{C}$, where $c(t)$ is the instantaneous concentration, C_{min} is the minimum concentration in the dataset, $\overline{C}$ is the mean concentration.

The analytical distributions that we tested to fit the experimental PDFs are the ones proposed in literature studies as suitable for modeling the dispersion of a passive scalar within an atmospheric boundary layer: the Lognormal distribution, the Gamma distribution and the Weibull 2p distribution. To adapt the models to the experimental data, the scale and the shape parameters have been estimated applying the methods of moments, which states that the mean and the variance of the analytical distribution are equal to the ones of the experimental distribution ($\overline{c}$ and σ_c^2, respectively). Below, we report the analytical expressions:

1. Gamma distribution

$$P(c,\kappa,\vartheta) = \frac{1}{\Gamma(\kappa)\cdot\vartheta}\left(\frac{c}{\vartheta}\right)^{\kappa-1} exp\left(-\frac{c}{\vartheta}\right) \tag{3.6}$$

where c is the instantaneous concentration, $\Gamma(\cdot)$ is the Gamma function, κ is the shape parameter and ϑ it the scale parameter. The scale and the shape parameters are calculated as:

$$\begin{cases} \overline{c} = \kappa\cdot\vartheta \\ \\ \sigma_c^2 = \kappa\cdot\vartheta^2 \end{cases} \longrightarrow \begin{cases} \kappa = \frac{\overline{c}^2}{\sigma_c^2} = i_c^{-2} \\ \\ \vartheta = \frac{\sigma_c^2}{\overline{c}} \end{cases} \tag{3.7}$$

where i_c is the fluctuation intensity parameter.

2. Lognormal distribution

$$P(c,\mu_l,\sigma_l) = \frac{1}{c\sigma_l\sqrt{2\pi}} exp\left(-\frac{(ln(c)-\mu_l)^2}{2\sigma_l^2}\right) \tag{3.8}$$

where μ_l and σ_l are respectively the mean and the standard deviation of the Lognormal distribution, and they are calculated as:

$$\begin{cases} \mu_l = ln(\overline{c}^2/\sqrt{\sigma_c^2+\overline{c}^2}) \\ \\ \sigma_l = \sqrt{ln(\sigma_c^2/\overline{c}^2+1)} \end{cases} \tag{3.9}$$

3. Weibull 2p distribution

$$P(c,a,b) = \frac{b}{a}\left(\frac{c}{a}\right)^{b-1} exp\left(-\left(\frac{c}{a}\right)^b\right) \tag{3.10}$$

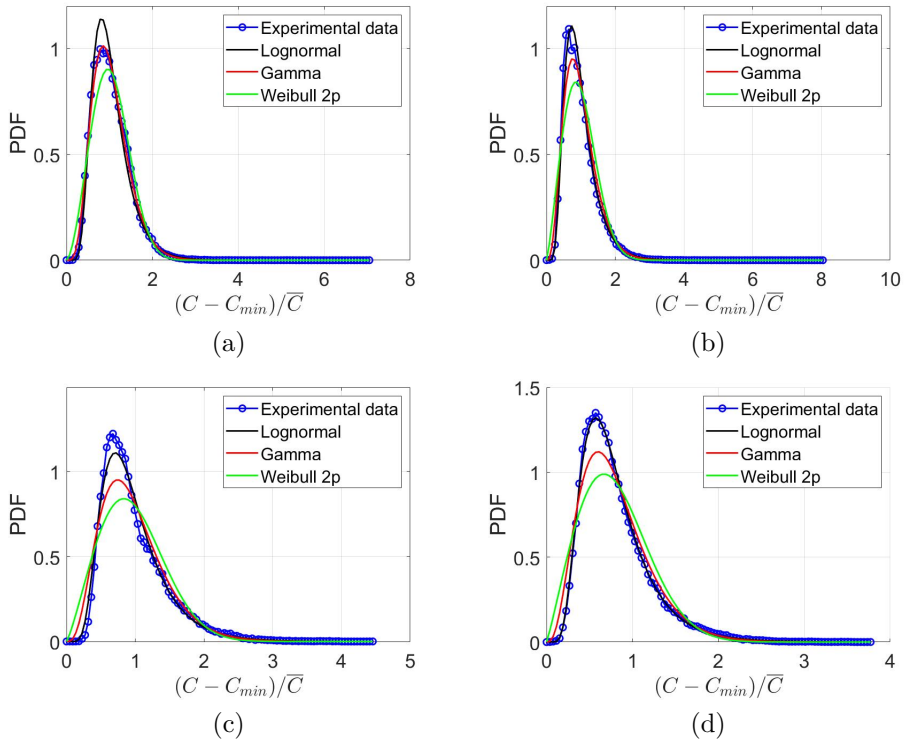

Figure 3.18: *(a) PDF at Y=0 mm. Zero configuration; (b) PDF at Y=-50 mm. One-tree configuration; (c) PDF at Y=-25 mm. Half configuration; (d) PDF at Y=-50 mm. Full configuration.*

where a is the scale parameter and b is the shape parameter, calculated as:

$$\begin{cases} a = \frac{\overline{c}}{\Gamma(1+\frac{1}{b})} \\ b = \left(\frac{\overline{c}}{\sigma_c}\right)^{1.086} = \left(\frac{1}{i_c}\right)^{1.086} \end{cases} \tag{3.11}$$

Once the distribution parameters are estimated, the analytical models are applied by adopting the same sample discretization used to calculate the experimental PDFs. Below we show the comparison between experimental PDFs and analytical ones, estimated in positions that correspond to the minimum (figure 3.18) and to the right peak (figure 3.19) of the mean concentration profiles (see figure 3.17). We chose to show the PDFs obtained in correspondence of the minimum and on the peack, because we expect different shapes of the PDFs where the concentration changes the most among the four configurations. As a first qualitative observation, we can say that there is not a great difference in the shapes of the PDFs, and that

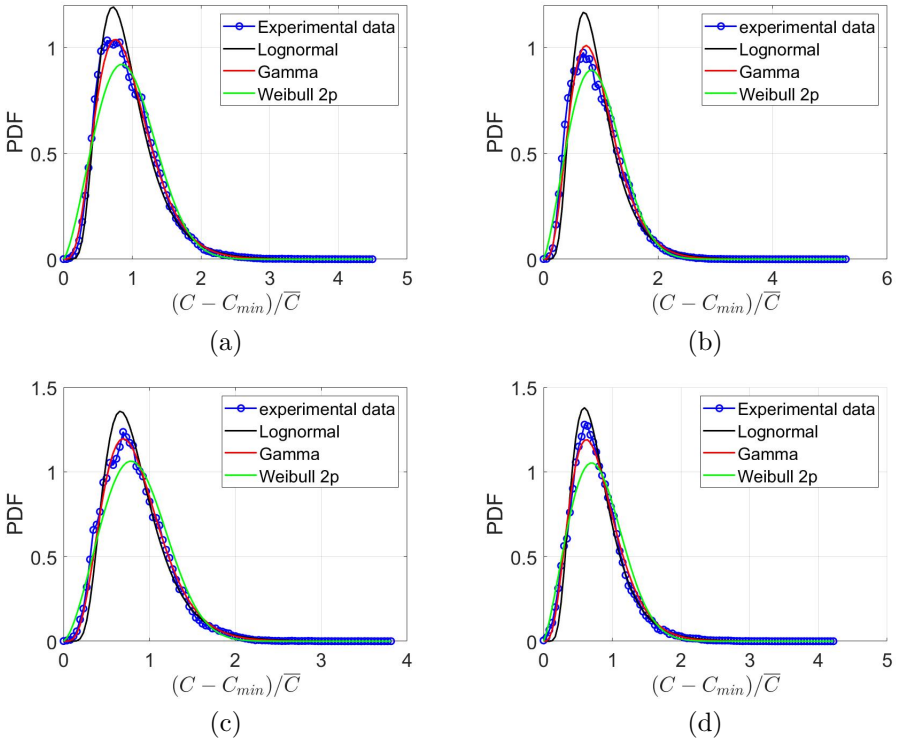

Figure 3.19: *(a) PDF at Y = 200 mm. Zero configuration; (b) PDF at Y = 150 mm. One-tree configuration; (c) PDF at Y = 100 mm. Half configuration; (d) PDF at Y = 200 mm. Full configuration.*

the Lognormal distribution and the Gamma distribution have good agreement with the shape of the experimental PDFs.

To characterize the shape of the PDFs, the third and the fourth moments have been studied. The third order moment (M_3), or skewness, measures the asymmetry of the PDF: positive skewness indicates that the right tail is the dominant tail of the distribution, negative skewness indicates that the left tail is dominant. The fourth order moment (M_4), or kurtosis, represents the shape of the tails of the PDF, which is linked to the amount of extreme events in the concentration time series. High kurtosis implies a higher probability of finding values far from the mean, leading to higher intermittency of the signal. The skewness and the kurtosis of experimental PDF have been calculated applying their definition:

$$M_n = \frac{\frac{1}{N}\sum_{i=1}^{N}(c_i - \overline{c})^n}{\sigma_c^n} \tag{3.12}$$

where N is the total number of samples, c_i is the instantaneous concentration, $\overline{c}$ is the mean concentration, σ_c is the concentration standard deviation, $n = 3, 4$ indicates the moment order. In figure 3.20 the trend of the skewness and the kurtosis along the canyon is reported. Both moments present a constant behavior, as we have observed for the fluctuation intensity (figure 3.8). It means that in different spatial points the PDFs have similar shapes. Moreover, we observe that the homogeneity increases in the configurations with trees, as their statistical moments' profiles do not present outliers (red and back lines in figure 3.20). The skewness profiles show that the PDFs are skewed to the right. The kurtosis is higher than 3, thus the distributions have longer tails with respect to a Gaussian distribution. It is close to 9, which is the kurtosis of the exponential distribution.

The goodness of the fitting between the experimental PDF and the model PDF is evaluated by applying statistical tests. The Kullback-Leibler divergence test (retrieved from Orsi et al. (2021)) and the Kolmogorov-Smirnov test have been used. The Kullback-Leibler divergence test (KL test) evaluates the goodness of fitting by measuring the divergence between the experimental PDF from the model PDF. It is defined as:

$$D_{KL}(p||q) = -\sum p \cdot log_2\left(\frac{p}{q}\right) \tag{3.13}$$

where p is the experimental PDF and q is the model PDF. The condition that has to be verified to have good fitting is $p/q \to 1$, therefore $D_{KL} \to 0$. The Kolmogorov-Smirnov goodness-of-fit test (KS test) measures the maximum absolute difference between the experimental Cumulative Distribution Function (CDF) and the analytical one. It is defined as:

$$D_n = sup(|CDF_{experimental} - CDF_{model}|). \tag{3.14}$$

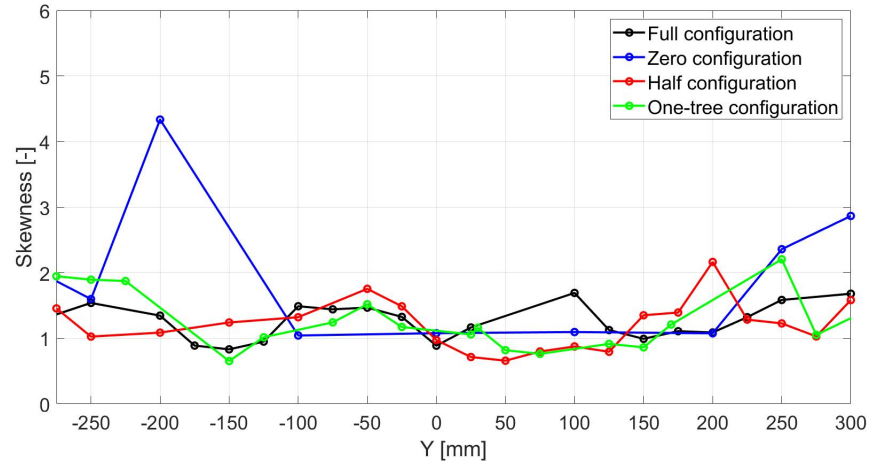

(a)

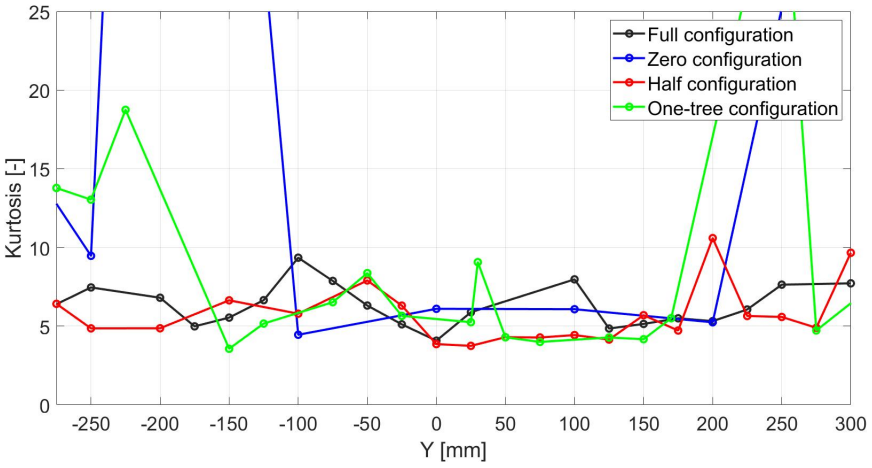

(b)

Figure 3.20: *Longitudinal profiles of (a) experimental skewness; (b) experimental kurtosis.*

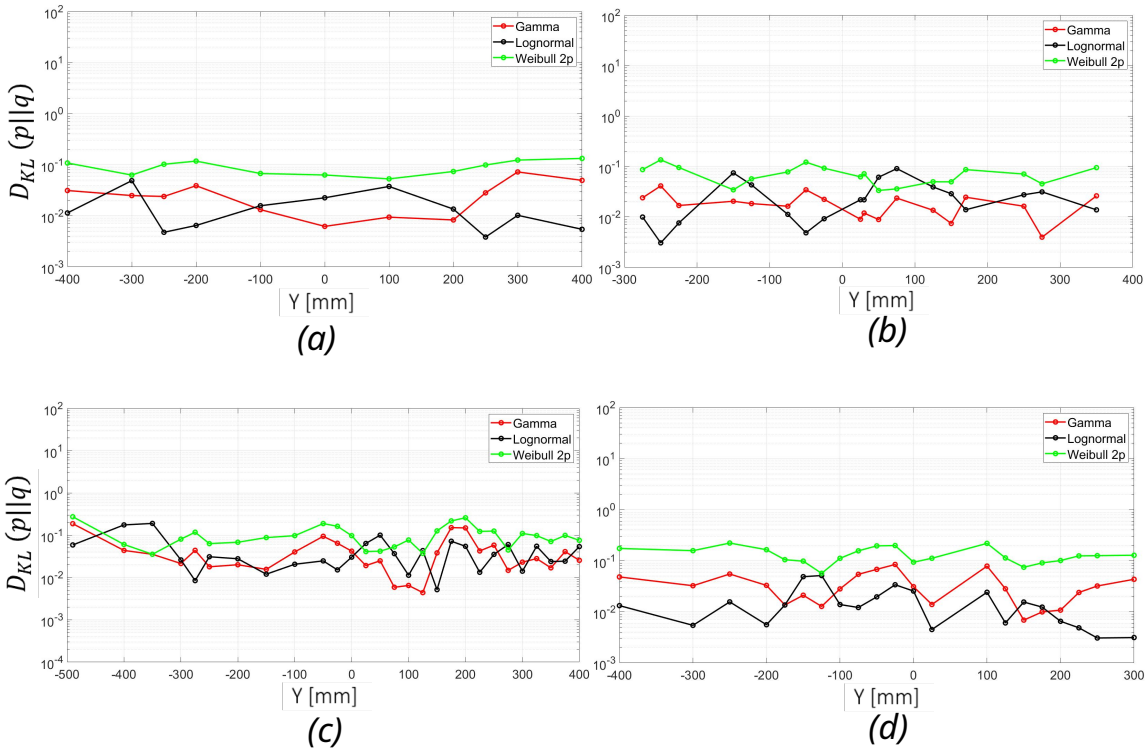

Figure 3.21: *Profiles of the results of the KL test. (a) Zero configuration; (b) One-tree configuration; (c) Half configuration; (d) Full configuration.*

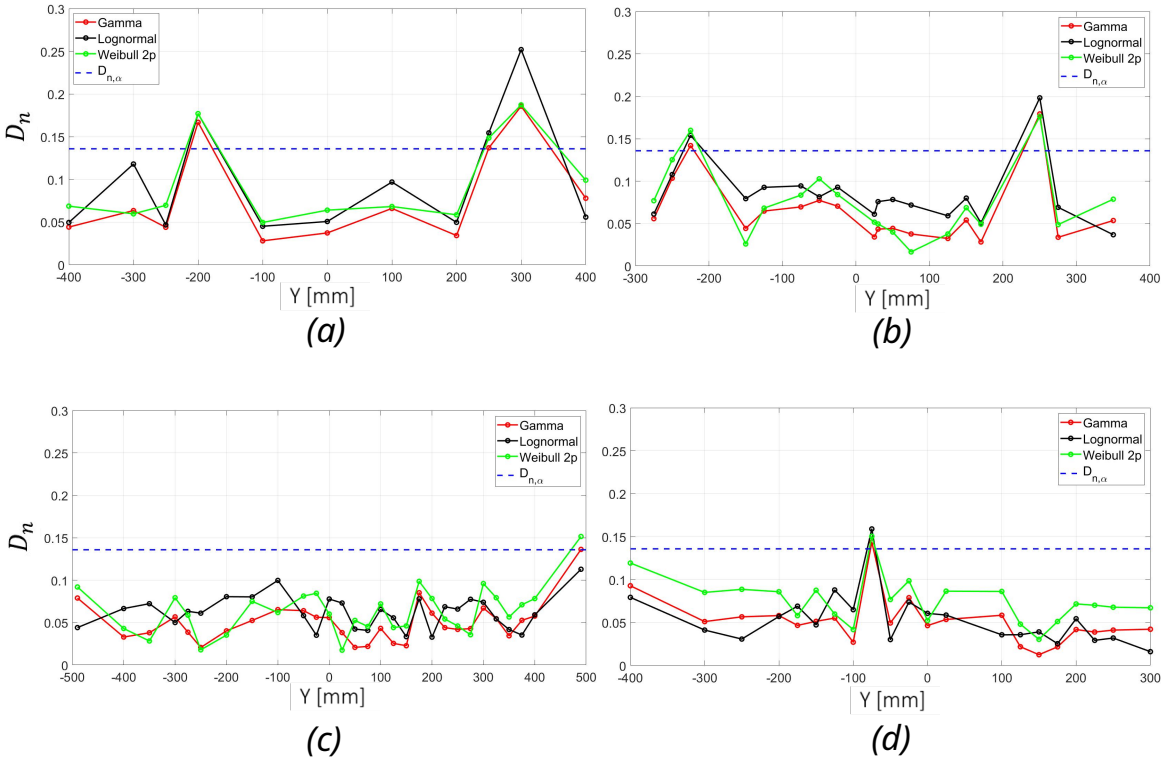

Figure 3.22: *Profiles of the results of the KS test. (a) Zero configuration; (b) One-tree configuration; (c) Half configuration; (d) Full configuration.*

The result of the test has to be compared with a critical value, which is defined as the largest theoretic difference acceptable at a certain significance level (α). If we consider α=0.05, the critical value is computed as:

$$D_{n,\alpha} = \frac{1.36}{\sqrt{n}} \tag{3.15}$$

where n is the number of samples, here equal to 100. Therefore, if $D_n < D_{n,\alpha}$, the hypothesis that the experimental data can be described with the tested analytical distribution is accepted at 5% significance level. The tests have been applied three times to evaluate the quality of the fitting of the Gamma, Lognormal and Weibull 2p distributions to the experimental PDFs, at each point of the longitudinal profiles. The profiles of the KL test (figure 3.21) tend to zero and they show higher values for the Weibull 2p distribution. The profiles of the KS test (figure 3.22) lay below the threshold almost everywhere for the configurations with trees, and with the exception of a few points in the Zero and One-tree configurations. Therefore, the three analytical models are suitable to describe the dispersion phenomenon which develops inside the canyon, according to both tests.

Even if the statistical tests show good fitting for all the analytical distributions, the Gamma distribution can be considered the best model for pollutants dispersion, as it is suitable even if we want to change the geometry of the pollutant source, for example putting a point source rather than a linear one. Moreover, it allows us to characterize the dispersion phenomenon within the canyon knowing a single parameter, namely the fluctuation intensity. The Lognormal distribution performs a good fitting of the experimental PDF as well, as inside the canyon there is a linear source, thus there is no meandering. Also having assessed the goodness of the Weibull 2p distribution is an important result, as it provides an analytical expression to calculate the percentiles of the experimental CDF (Oettl and Ferrero, 2017).

3.2.2 Study of the right tails of the concentration PDF

In this section we focus the statistical analysis on the tails of the PDFs, to properly model extreme concentration events, that play an important role in the air quality assessment. By evaluating the third and the fourth moments of the concentration time series we have observed that the experimental PDFs are skewed to the right, and they have heavy tails. Therefore, it is interesting to investigate if the right tails of the experimental PDFs decay with an exponential law or with a power law. If the tail can be fitted with an exponential law, it can be modeled using an exponential function, whose shape is governed by one parameter (the inverse of the mean of the experimental data). On the contrary, if the tails decay with a power law, the phenomenon cannot be represented with basic statistics, thus superstatistical methods have to be recalled (Beck et al., 2005; Williams et al., 2020).

In the present work, the tails of the experimental PDFs have been defined as the part of the PDF which contains 10% of the concentration data. In other words, it is the area under the PDF over the 90^{th} percentile. We isolated the tails and we plotted them on a semilogarithmic graph, knowing that they are exponential if they show a linear behavior on a semilogarithmic plot, otherwise they are power law tails. It has been observed that all the experimental tails lay on a straight line almost entirely, except for a few points in the bottom part, negligible as they are associated to low levels of probability. We concluded that the experimental PDF tails can be fitted with an exponential law of type:

$$y = ae^{-ax} \tag{3.16}$$

where the independent variable x stands for the concentration data contained in the PDF tail, the dependent variable y stands for the associated probability and the a parameter is obtained performing a best fit between the exponential law and the experimental data. The exponential tail fitting has been performed using the Matlab function "fit", which fits the experimental data with the nonlinear model

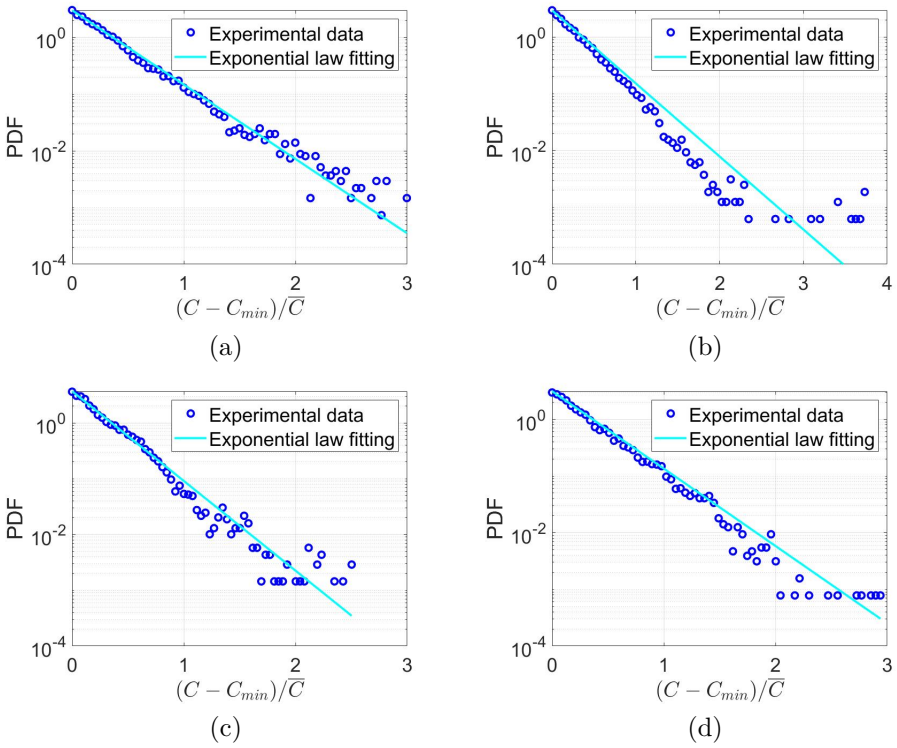

Figure 3.23: *(a) PDF tail at Y=200 mm. Zero configuration; (b) PDF tail at Y=150 mm. One-tree configuration; (c) PDF tail at Y=100 mm. Half configuration; (d) PDF tail at Y=200 mm. Full configuration.*

reported in equation 3.16, on a normal scale plot. The Least Squares Method was not used, because it requires the linearization of the exponential function, which gives greater weight to the low probability values, thus the fitting would be governed by the part of the tail that deviates from the linearity. To visualize the result of the nonlinear fitting procedure we report, in figure 3.23, the tails of the PDFs, which were reported in figure 3.19. To have a global visualization of the variation of the shape of the tails in different spatial points, we report the variation of the a parameter with respect to Y (figure 3.24). The smaller is a the longer is the tail of the PDF. We cannot identify a clear trend in the variation of a along Y, in line with what we have found in the analysis of skewness and kurtosis of the global PDFs: their longitudinal behavior was quite constant along Y. It implies that the tails of the experimental PDFs have similar shapes. Moreover, we can notice that the mean of the values of the a parameter of the Full configuration (black dotted line) is the highest one. It means that the PDFs calculated in the Full configuration show shorter tails, or rather less extreme events, that demonstrates that the presence of a high number of trees homogenizes the concentration signal.

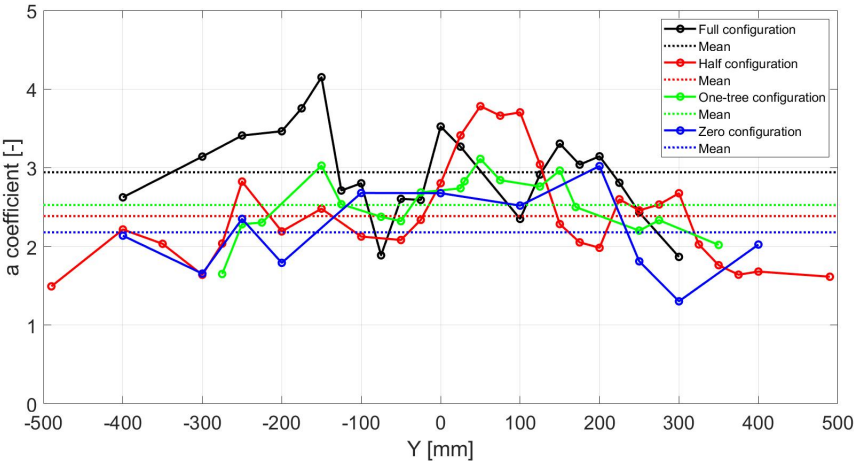

Figure 3.24: *Spatial variation of the a parameter contained in the exponential law function (equation 3.16).*

The goodness of the fitting of the exponential law has been evaluated with the KS test. The quality of the fitting is assessed by comparing the distance between the exponential CDF and the experimental one, with the critical threshold defined in equation 3.15. As the threshold depends on the number of samples, which varies from one PDF tail to another, the threshold is not unique. In order to refer to a common threshold, we report the P-Value. The P-Value is the probability associated to the results of the test (namely, the maximum distance between the experimental CDF and the model CDF), obtained assuming that the hypothesis that the exponential law is suitable for the experimental data is true. It is calculated by extracting α imposing the condition $D_n < D_{n,\alpha}$. It is necessary to develop the numerator of the threshold equation so that equation 3.15 becomes:

$$D_n > \frac{\sqrt{-\frac{1}{2} \cdot ln(\frac{\alpha}{2})}}{\sqrt{n}} \tag{3.17}$$

where D_n is the maximum difference between the exponential CDF and the experimental one, n is the number of samples contained in the tail. By rearranging the terms we can obtain the equation for α:

$$\alpha < 2 \cdot e^{-2nD_n^2}. \tag{3.18}$$

The obtained P-Value (plotted in figure 3.25) is compared with an assumed level of significance, here 0.05: if it is higher we can accept the hypothesis of the good fitting. We can summarise the results reported in figure 3.25 by reporting the fraction of the total points in which the P-Value is greater than α: it is higher in the Half and

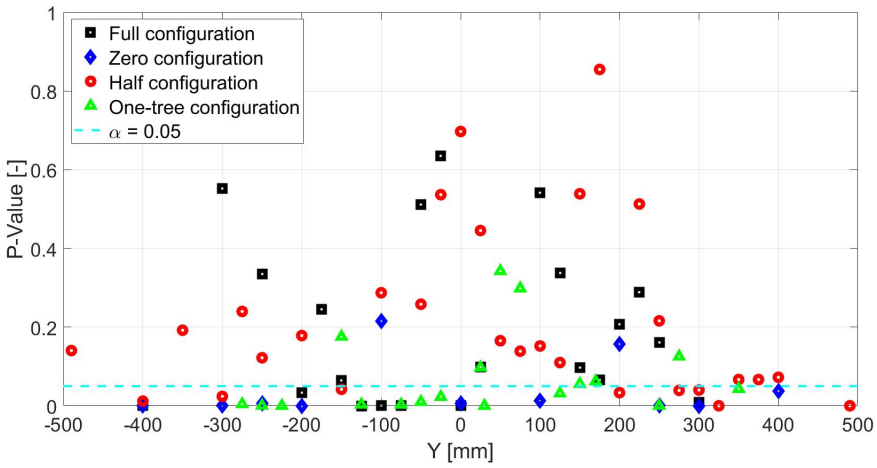

Figure 3.25: *Spatial variation of the P-Value of the KS test, applied to assess the goodness of the fitting of the exponential law to the tails of the experimental PDFs.*

Full configurations, respectively 0.72 and 0.67, and lower for the Zero and One-tree configurations, respectively 0.18 and 0.39. It shows that the exponential law is more suitable to model the tails of the PDFs calculated for the configurations with trees.

3.2.3 Analysis of the autocorrelation of the concentration time series

In the time series analysis, another important parameter to be studied is the autocorrelation of the concentration signal. The autocorrelation function denotes the linear relation between the concentration at time t and the concentration at time $t + dt$, where dt are progressively larger time lags. It is defined as:

$$R(dt) = \frac{\frac{1}{N}\sum_{t=1}^{N-dt}(c(t) - \overline{c}) \cdot (c(t + dt) - \overline{c})}{\sigma_c^2} \tag{3.19}$$

where c is the concentration at the time t and $t + dt$, t is the acquisition time, dt is the time lag, N is the total number of samples (300 000 each spatial point), σ_c^2 is the total variance. The concentration values are used in their non-dimensional form $C/\overline{C}$ (where C is the instantanoeus concentration and $\overline{C}$ is the average concentration), to compair the different autocorrelograms.

The variation of the autocorrelation of the concentration time series with respect to dt is visualized by plotting autocorrelograms. In turbulent flows, the autocorrelation decreases as the time lag increases, until a value beyond which the autocorrelation fluctuates around zero, as for large time lags turbulence loses linear memory and it is a random phenomenon. The total area under the autocorrelogram

Table 3.2: *P-value of the T-Student test, applied to the time lag profiles for the two autocorrelation tresholds.*

R = 0.2	**Full conf.**	**Half conf.**	**One-tree conf.**	**Zero conf.**
Full conf.	-	0.54	0.30	0.11
Half conf.	-	-	0.28	0.13
One-tree conf.	-	-	-	0.43
Zero conf.	-	-	-	-
R = 0.6				
Full conf.	-	0.69	0.56	0.004
Half conf.	-	-	0.52	0.13
One-tree conf.	-	-	-	0.02
Zero conf.	-	-	-	-

defines the dominant time scale of the process. As the numerical computation of the integral scale can be affected by non-negligible errors, the autocorrelation of the signal is evaluated by extracting the time lags at which the autocorrelation function falls below two thresholds: 0.6, as the high correlation threshold and 0.2, as the low correlation threshold. The calculation of the autocorrelation function, and the extraction of the times lags that correspond to the thresholds, have been carried out for all time series, acquires in the points of the profiles shown in figure 3.17.

The obtained time lags are visualized on profiles along the Y direction, to verify if the temporal correlation of the fluctuating concentration signals depends on the space or on the tree density (figures 3.26a, 3.26b). The time lag profiles do not present a clear spatial trend in any configuration, which means that the dispersion phenomenon inside the canyon is not characterized by different processes that are governed by largely different time scales. However, we can notice that the mean value of the time lag profile in the Zero configuration (blue dotted line) is the lowest one if both the thresholds are observed.

As the profiles present fluctuations around the mean values, the T-Student test has been applied to verify if the differences between the mean values are statistically significant. We read the results of the test by comparing the P-Value with the level of significance (again, α=0.05). If P-value$<\alpha$ the hypothesis of equal means is rejected and we can state that the difference between the means is statistically significant. The datasets involved in the comparison have different sizes and different variances. All the different combinations of tests among the different configurations are reported in Table 3.2. The mean of the lag time profiles of the Zero configuration is significantly lower than the ones of the Full and One-tree configuration if the higher autocorrelation threshold is considered (respectively the P-Value is 0.004 and

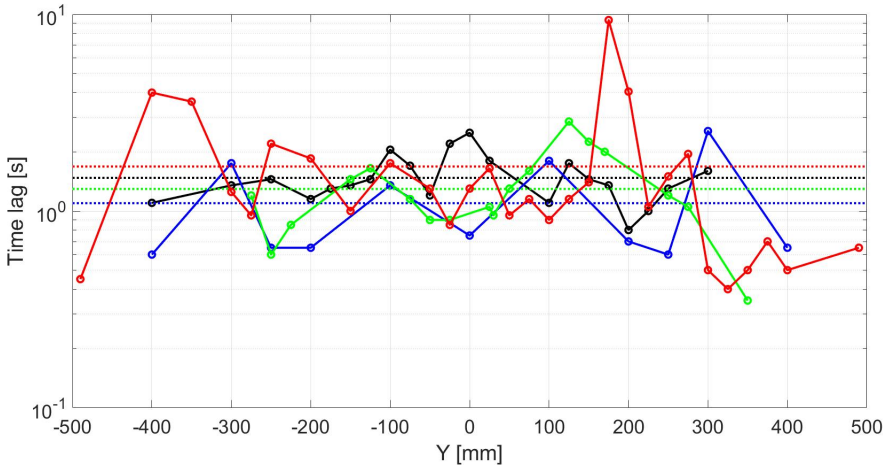

(a)

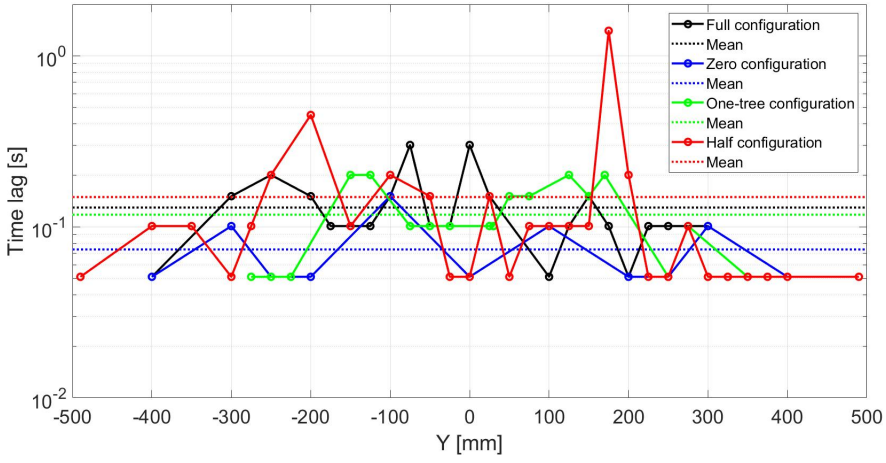

(b)

Figure 3.26: *(a) Profiles of the time lag at which the autocorrelation is equal to 0.2; (b) profiles of the time lag at which the autocorrelation is equal to 0.6.*

0.02). However, there is no significant difference between the means of the profiles of the time lags which correspond to the low threshold value. We can conclude that the linear memory of the concentration signal is increased by the presence of trees, only if the high autocorrelation threshold is considered.

3.2.4 Spectral analysis of the time series of turbulent mass and momentum fluxes

Mass and momentum transfer within turbulent flows are governed by turbulent structures of different dimensions. To investigate the length scales of the turbulent structures which dominate the two transport mechanisms within the street canyon (both empty and vegetated), it is necessary to analyze the time series of turbulent mass flux ($w'c'(t)$) and Reynolds stresses ($u'w'(t)$), respectively, in the frequency domain. With this aim, spectral analysis has been performed. The Power Spectral Density (PSD) is calculated by applying the Fourier transform to the autocorrelation function of the fluctuating signal. The Fourier transform operates on a signal sampled with a constant frequency. As the velocity components have been acquired with the LDA, the sampling frequency of $u'(t)$ and $w'(t)$, and consequently of the coupled signals, is not constant, therefore, it is necessary to post-process both $w'c'(t)$ and $u'w'(t)$ time series. We have defined a constant sampling frequency (f_s) of 1000 Hz, as it corresponds to the acquisition frequency of the FID, and during the coupled measurement campaign we have forced both the FID and the LDA to have the same acquisition frequency (as we have explained in section). Concerning the $w'c'(t)$ signal, we applied the S+H method to calculate the time shift which maximizes the correlation between concentration and velocity signals (the technique has been illustrated in section 2.2.3), and then we resampled both signals on the constant frequency, f_s. The $u'w'(t)$ signal has been obtained from the correlation between the streamwise velocity fluctuations ($u(t)$-$\overline{u}$, where $u(t)$ is instantaneous velocity and $\overline{u}$ is the mean velocity) and the vertical velocity fluctuations ($w(t)$-$\overline{w}$, where $w(t)$ is instantaneous velocity and $\overline{w}$ is the mean velocity). They have been acquired simultaneously, using the LDA coupled with the mirror (used to obtain the vertical velocity component, see section 2.2.2), thus only the resampling on f_s of the two signals has been performed.

Once we have obtained two signals sampled on a constant frequency, the PSD has been calculated by applying the Welch's method, in order to obtain smooth spectra. According to this method, the time series is divided into N number of windows and the Fourier transform of the autocorrelation function of the signal is calculated for each window. The final spectrum is the mean of the spectra calculated in each window. We have to consider that a high number of windows provides a smoother spectrum, but the time window where we compute the Fourier transform is reduced, hence the information about low-frequency components is lost. As low-

frequency components are representatives of large-scale structures it is important to not lose their information. It has been verified that dividing the time series in windows of 1000 samples is a good compromise between the resolution of the spectrum and the information about low-frequency components. To each window, the Hamming filter has been applied. Before computing the spectrum, the mean and the trend component have been subtracted from the $w'c'(t)$ and $u'w'(t)$ time series, to remove strong periodic components that may appear as fictitious peaks at low frequencies. The PSD of $w'c'(t)$ (called $S_{w'c'}$) and of $u'w'(t)$ (called $S_{u'w'}$) is interpreted as the contribution of turbulent structures of different frequencies to the total variance of the fluctuating signal. In particular, low frequencies are representative of large-scale structures, and large frequencies are representative of small-scale structures. Premultiplied spectra are reported, to preserve the property that the area below the curve is proportional to the energy content of the signal, therefore, a peak in the premultiplied spectra represents the energetic contribution of a turbulent structure of a certain size.

We show the spectra calculated at the rooftop of the canyon, in correspondence of the minimum concentration area (so on the central axis of the canyon at Y=0 mm) and of the maximum concentration area (at Y=200 mm). We report the Zero configuration with the Full configuration, in order to understand which turbulent scale dominates mass and momentum transfer in the empty and vegetated canyon. Both the PSD and the associated frequencies are reported in non-dimensional form, following the model of Kaimal et al. (1972). The non-dimensional PSD is reported as:

$$\frac{S_{w'c'} \cdot f_s}{\sigma_w \sigma_c}, \qquad \frac{S_{u'w'} \cdot f_s}{\sigma_u \sigma_w} \tag{3.20}$$

where $S_{w'c'}$ is the PSD of $w'c'(t)$, $S_{u'w'}$ is the PSD of $u'w'(t)$, f_s is the constant sampling frequency, σ_w is the standard deviation of the vertical velocity signal, σ_c is the standard deviation of the concentration signal, σ_u is the standard deviation of the streamwise velocity signal. The non-dimensional frequency is repoted as:

$$n = \frac{f \cdot W}{u_*} \tag{3.21}$$

where f is the dimensional frequency, W is the width of the canyon and u_* is the friction velocity. In figure 3.27 we report the premultiplied spectra of the turbulent mass flux, at the rooftop. Looking at the low frequencies, associated to large-scale structures, we can notice that they give a higher contribution to the total energy of the signal in the Zero configuration, meaning that the contribution of the large-scale structures to the turbulent mass fluxes is higher when trees are not present in the canyon. We observe the same result in the spectra of Reynolds stresses, reported in figure 3.28. Looking at the peaks of the spectra, which identify the frequencies that contribute more to the total energy of the signal, we can observe that the

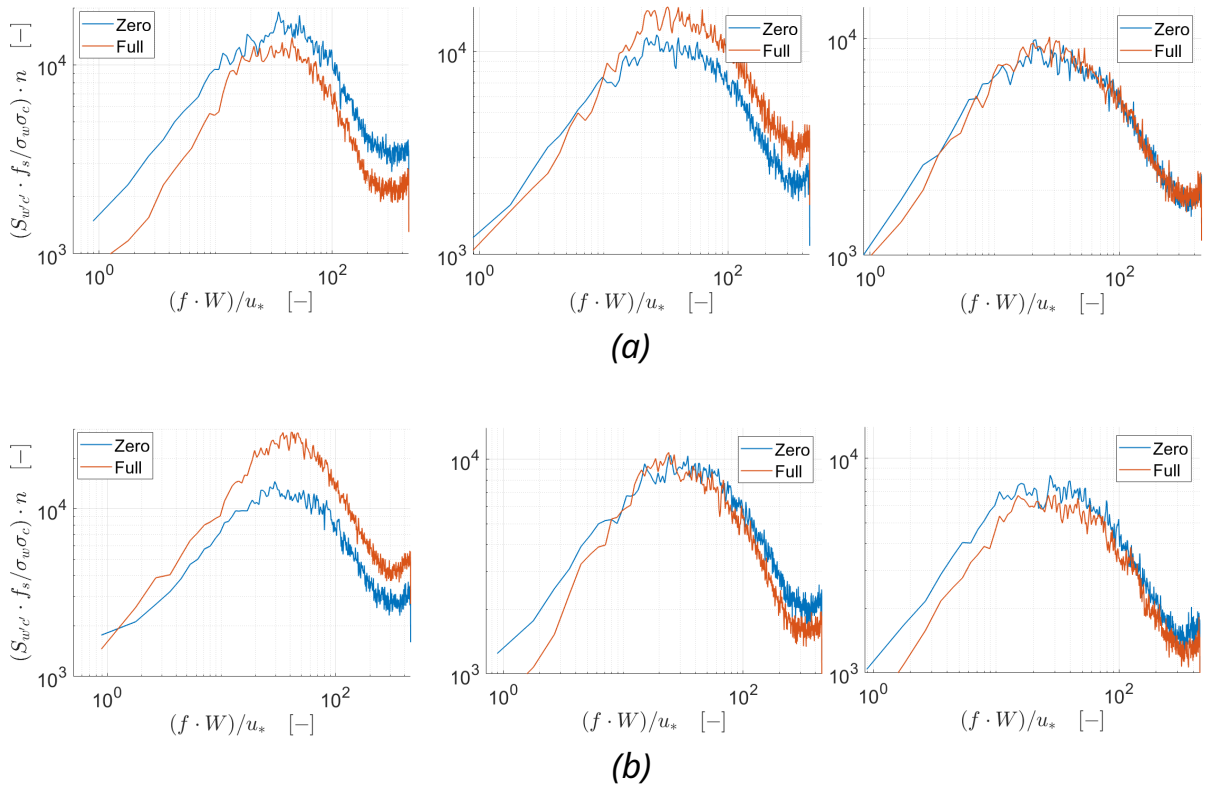

Figure 3.27: *Premultiplied power spectra of turbulent mass fluxes at the rooftop, at X=50 mm close to the upwind wall (left), at X=100 mm in the center of the canyon (center), at X=150 mm close to the downwind wall (right). (a) Y=0 mm; (b) Y= 200 mm.*

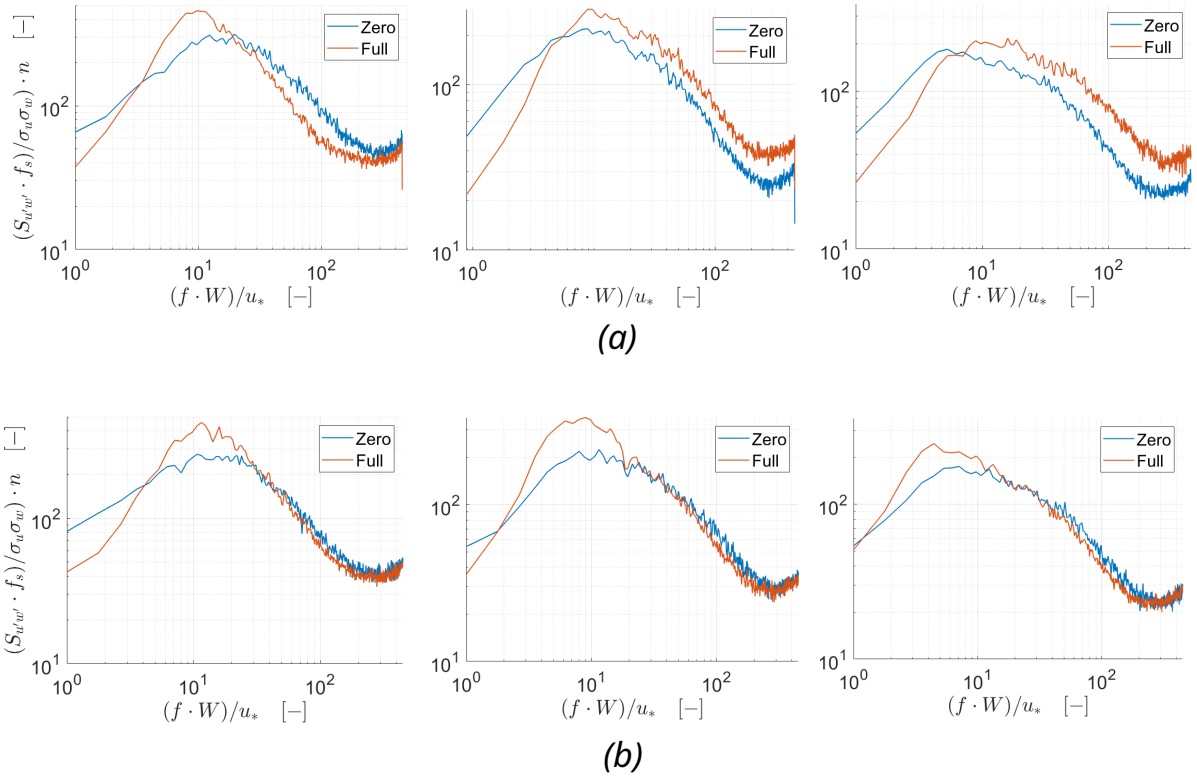

Figure 3.28: *Premultiplied power spectra of Reynolds stresses at the rooftop, at X=50 mm close to the upwind wall (left), at X=100 mm in the center of the canyon (center), at X=150 mm close to the downwind wall (right). (a) Y=0 mm; (b) Y= 200 mm.*

size of the turbulent structures is the same in both configurations for the PSD of $w'c'(t)$, while looking at the PSD of $u'w'(t)$ we can notice that the peak of the spectra in the Full configuration is shifted towards higher frequencies with respect to the one in the Zero configuration, especially in the center of the canyon moving towards the downwind wall (figure 3.28a). From this observation, we can hypnotize that in presence of trees moving toward the downwind wall small-scale turbulent structures are responsible for turbulent momentum transfer. The final part of the spectra, where the Power Spectral Density becomes constant with the increase of the frequency, is defined as "white noise", and it has to be neglected. It is expected that small-scale structures have higher energy in the vegetated canyon, and that large-scale structures have higher energy in the empty canyon, but this hypothesis has not been completely verified by the spectral analysis.

Chapter 4

Conclusions

The aim of the present work was to investigate the impact of tree avenues on the ventilation and pollutant dispersion in an urban street canyon. These subjects have been investigated through an experimental campaign performed inside the wind tunnel of École Centrale the Lyon. Concentration, velocity, and combined concentration and velocity measurements have been performed inside a street canyon, modeled as a closed cavity oriented perpendicular to the wind direction, inserted in an urban network reproduced inside the test section. Four different tree density configurations were considered: an empty canyon (Zero configuration), a canyon with two rows of one tree (One-tree configuration), a canyon with two rows of seven trees (Half configuration), and a canyon with two rows of fourteen trees (Full configuration). A mixture of ethane and air has been used as a tracing substance to characterize the pollutant transport inside the canyon.

The results show that the presence of trees inside the street canyon determines the transition from a two-dimensional concentration field (characteristic of the Zero configuration) to a clearly three-dimensional one (characteristic of the Hal and Full configurations). Indeed, the concentration is homogeneous along the longitudinal direction of the canyon in the Zero configuration, while, when trees are inserted, the concentration field becomes heterogeneous, with areas of accumulation of pollutant and areas of low concentration. The ventilation efficiency of the canyon is not affected by the vegetation density, as we have observed that the vertical exchange velocity is almost constant among the four configurations.

The mean velocity field is almost two-dimensional, as the lateral velocity component is almost zero. It seems that the presence of trees homogenizes the vertical mean velocity, but this result is not representative, because in the center of the canyon (where velocity measurements were acquired) the vertical velocity is low with respect to the one that would be measured at the walls. From the velocity fluctuations, we calculated the turbulent kinetic energy and it emerged that it decreases with the increase of the density of vegetation. However, it is not responsible

for the decreasing of the ventilation efficiency in the fully vegetated canyon (where the TKE is close to zero), as the mean flow dominates the pollutant dispersion inside a canyon whose aspect ratio is 0.5.

Concerning the turbulent mass fluxes, a strong negative turbulent mass flux inside the empty canyon is probably responsible for the concentration mixing in this configuration, but it does not improve the ventilation efficiency, as it does not enhance the vertical transport of the pollutant outside the canyon. A quadrant analysis of the turbulent mass fluxes at the rooftop of the canyon revealed that the vertical pollutant transport is dominated by the entrance of clean air, and its local contribution with respect to the total contributions of all quadrants is homogeneous along the canyon with and without vegetation.

The statistical analysis of concentration time series reveals that the Lognormal, the Gamma and the Weibull 2p are suitable analytical distributions to model pollutant dispersion inside the canyon. The PDF of the concentration time series is positively skewed and its tail decays with an exponential law.

This experimental campaign highlights the complexity of the aerodynamic effect of tree avenues displaced inside an urban street canyon, on the flow structures. The fine three-dimensional measurement grid used for the acquisition of concentration measurements provides a complete characterization of the behavior of the pollutant dispersion, both inside an empty canyon and a vegetated one. The results highlight that vegetation modifies the concentration field, but does not hinder the overall ventilation of the canyon. Having found that the u_d parameter does not depend on the vegetation density, allowed us to insert it, as a constant parameter, inside parametric models that simulate pollutant dispersion in the urban environment (for example SIRANE model developed by Soulhac et al. (2011)). The huge database of concentration data can be used for the validation of numerical models. Moreover, further experimental campaigns can be carried out to analyze the influence of other parameters on pollutant dispersion. For example, we could repeat the same experimental campaign inside a narrower cavity, or we can change the geometry and the displacement of the trees, for example inserting smaller trees or translating the two tree rows in the center of the canyon.

Bibliography

Abhijith, K., Kumar, P., Gallagher, J., McNabola, A., Baldauf, R., Pilla, F., Broderick, B., Di Sabatino, S., and Pulvirenti, B. (2017). Air pollution abatement performances of green infrastructure in open road and built-up street canyon environments–a review. *Atmospheric Environment*, 162:71–86.

Balestrieri, G. (2021). *Influence of vegetation on vertical mass exchange velocity in urban street canyon*. PhD thesis, Politecnico di Torino.

Beck, C., Cohen, E. G., and Swinney, H. L. (2005). From time series to superstatistics. *Physical Review E*, 72(5):056133.

Buccolieri, R., Gromke, C., Di Sabatino, S., and Ruck, B. (2009). Aerodynamic effects of trees on pollutant concentration in street canyons. *Science of the Total Environment*, 407(19):5247–5256.

Cancelli, C., Boffadossi, M., and Salizzoni, P. (2006). *Fluidodinamica ambientale: Turbolenza e dispersione*. Otto Editore.

De Giovanni, A. (2019). *Assessment of the impacts of trees on pollutants dispersion in urban canopy by means of a wind tunnel study*. PhD thesis, Politecnico di Torino.

Di Bernardino, A., Monti, P., Leuzzi, G., and Querzoli, G. (2018). Pollutant fluxes in two-dimensional street canyons. *Urban climate*, 24:80–93.

F Yassin, M. (2008). Probability characteristics of concentration fluctuations in plume dispersal. *JES. Journal of Engineering Sciences*, 36(1):115–130.

Fellini, S. (2021). *Modelling pollutant dispersion at the city and street scales*. PhD thesis, École Centrale de Lyon.

Fellini, S., Ridolfi, L., and Salizzoni, P. (2020). Street canyon ventilation: Combined effect of cross-section geometry and wall heating. *Quarterly Journal of the Royal Meteorological Society*, 146(730):2347–2367.

Ferrini, F., Fini, A., Mori, J., and Gori, A. (2020). Role of vegetation as a mitigating factor in the urban context. *Sustainability*, 12(10):4247.

Gromke, C., Buccolieri, R., Di Sabatino, S., and Ruck, B. (2008). Dispersion study in a street canyon with tree planting by means of wind tunnel and numerical investigations–evaluation of cfd data with experimental data. *Atmospheric Environment*, 42(37):8640–8650.

Gromke, C. and Ruck, B. (2007). Influence of trees on the dispersion of pollutants in an urban street canyon—experimental investigation of the flow and concentration field. *Atmospheric Environment*, 41(16):3287–3302.

Gromke, C. and Ruck, B. (2009). On the impact of trees on dispersion processes of traffic emissions in street canyons. *Boundary-Layer Meteorology*, 131(1):19–34.

Gromke, C. and Ruck, B. (2012). Pollutant concentrations in street canyons of different aspect ratio with avenues of trees for various wind directions. *Boundary-Layer Meteorology*, 144(1):41–64.

Irwin, H. (1981). The design of spires for wind simulation. *Journal of wind engineering and industrial aerodynamics*, 7(3):361–366.

Kaimal, J. C., Wyngaard, J., Izumi, Y., and Coté, O. (1972). Spectral characteristics of surface-layer turbulence. *Quarterly Journal of the Royal Meteorological Society*, 98(417):563–589.

Marro, M., Gamel, H., Méjean, P., Correia, H., Soulhac, L., and Salizzoni, P. (2020). High-frequency simultaneous measurements of velocity and concentration within turbulent flows in wind-tunnel experiments. *Experiments in Fluids*, 61(12):1–13.

Marucci, D. and Carpentieri, M. (2019). Effect of local and upwind stratification on flow and dispersion inside and above a bi-dimensional street canyon. *Building and Environment*, 156:74–88.

Mechinaud, L. (2021). Étude de l'effect de la présence d'arbres dans une rue sur la concentration en pollution.

Nironi, C., Salizzoni, P., Marro, M., Mejean, P., Grosjean, N., and Soulhac, L. (2015). Dispersion of a passive scalar fluctuating plume in a turbulent boundary layer. part i: Velocity and concentration measurements. *Boundary-layer meteorology*, 156(3):415–446.

Oettl, D. and Ferrero, E. (2017). A simple model to assess odour hours for regulatory purposes. *Atmospheric environment*, 155:162–173.

Oke, T. R. (2002). *Boundary layer climates*. Routledge.

Orsi, M., Soulhac, L., Feraco, F., Marro, M., Rosenberg, D., Marino, R., Boffadossi, M., and Salizzoni, P. (2021). Scalar mixing in homogeneous isotropic turbulence: A numerical study. *Physical Review Fluids*, 6(3):034502.

Salizzoni, P. (2006). *Mass and momentum transfer in the urban boundary layer*. PhD thesis, Ecully, Ecole centrale de Lyon.

Salizzoni, P., Marro, M., Soulhac, L., Grosjean, N., and Perkins, R. J. (2011). Turbulent transfer between street canyons and the overlying atmospheric boundary layer. *Boundary-layer meteorology*, 141(3):393–414.

Salizzoni, P., Soulhac, L., and Mejean, P. (2009). Street canyon ventilation and atmospheric turbulence. *Atmospheric Environment*, 43(32):5056–5067.

Soulhac, L., Salizzoni, P., Cierco, F.-X., and Perkins, R. (2011). The model sirane for atmospheric urban pollutant dispersion; part i, presentation of the model. *Atmospheric environment*, 45(39):7379–7395.

Tropea, C., Yarin, A. L., Foss, J. F., et al. (2007). *Springer handbook of experimental fluid mechanics*, volume 1. Springer.

Williams, G., Schäfer, B., and Beck, C. (2020). Superstatistical approach to air pollution statistics. *Physical Review Research*, 2(1):013019.

1